DEGREE PROJECT IN ENGINEERING PHYSICS,
SECOND CYCLE, 30 CREDITS
STOCKHOLM, *SWEDEN 2020*

Design of a compact wavefront sensor for measurements on the human eye

CHARLIE BÖRJESON

KTH ROYAL INSTITUTE OF TECHNOLOGY
SCHOOL OF ENGINEERING SCIENCES

Design of a compact wavefront sensor for measurements on the human eye

CHARLIE BÖRJESON

Supervisors: Linda Lundström & Dmitry Romashchenko

TRITA-SCI-GRU 2020:353
Department of Applied Physics

Abstract

Wavefront sensors for measurements on human eyes are usually large, expensive and difficult to move. A compact wavefront sensor would be more cost-effective and versatile as is could be used in multiple systems. The aim of this thesis was to produce a more compact and portable wavefront sensor.

A shorter telescope design for the wavefront sensor was proposed and checked theoretically and with computer simulations. An experimental arrangement comparing the proposed telescope design with a conventional telescope design was constructed. A compact wavefront sensor was built using off-the-shelf components and a few modified components. Tests with the compact wavefront sensor were made both on eye models and on human eyes.

The compact wavefront sensor correctly measured the refractive errors of two eye models. It was also possible to perform measurements on human eyes, both in the central and peripheral visual fields, and higher order aberrations were confirmed. For positioning human eyes at the correct distance from the wavefront sensor an additional pupil camera was needed, which was not included in the system. Future improvements for the compact wavefront sensor are discussed.

Contents

Abstract i

Contents ii

1 Introduction 1

2 Theoretical background 3
- 2.1 The human eye . . . 3
- 2.2 Aberrations . . . 4
- 2.3 Wavefront sensing . . . 6

3 Methods 13
- 3.1 Zemax simulations . . . 13
- 3.2 Test setup . . . 17
- 3.3 Final setup . . . 21
- 3.4 Evaluation tests . . . 26

4 Results and discussion 33
- 4.1 Eye model tests . . . 33
- 4.2 Human eye tests . . . 43
- 4.3 Future improvements . . . 44

5 Conclusion 47

Acknowledgement 49

Bibliography 51

A Derivation of ray transfer matrices 53

B Derivation of 2f-Kepler limit 57

C List of components in final setup 59

Chapter 1

Introduction

The most common reason for loss of visual image quality is imperfections in the optics of the eye. It is, however, difficult to get an objective measurement of the aberrations in the optics by asking a person about their perceived image quality while adding various corrective trial lenses, since the perceived image quality is also affected by various biological and psychological factors. Trial lenses only correct for defocus and astigmatism, so they can't be used to assess and correct additional higher order aberrations that also affect the image quality. To get an objective measurement of the optical quality of the eye that contains information about both lower and higher order aberrations, an wavefront sensor can be used.

The first paper [1] demonstrating the use of an ocular wavefront sensor was published in 1994. Since then, wavefront sensors have been extensively used to measure ocular aberrations. [2] Wavefront sensors that allow the test subject to have an open field of view are known as *open-field* wavefront sensors. Open-field wavefront sensors enable the test subject to use binocular vision and normal accommodation. The open field of view also allows the test subject to focus on a fixation target at a specific angle to the optical axis of the wavefront sensor, facilitating controlled measurements in the peripheral visual field. However, laboratory open-field wavefront sensors are often large, relying on long telescopes to allow for an open field-of-view for the test subjects. The telescope and other components such as an illuminating laser, pupil camera and sensor are placed individually along optical rails on a heavy optical table, making the system impossible to move without at least some re-alignment.

A smaller and more portable wavefront sensor would be advantageous, as it could be moved between different systems and locations. This would make it easier to measure on different populations at different locations, such as when studying how optical aberrations in the eye affect the development of myopia. Not needing to have multiple wavefront sensors would also reduce the total cost and size of these systems and provide greater flexibility for the scientists. The aim of this thesis was to design and build a relatively compact and portable open-field wavefront sensor.

Chapter 2

Theoretical background

In order to understand the principles of wavefront sensing we first need to get acquainted with the theory. This chapter will describe the optics of the human eye, as well as the function and principle of the components needed for eye wavefront sensing.

2.1 The human eye

The main optical elements of the eye are the cornea, the pupil, the lens and the retina, which can be seen in Figure 2.1. Light entering the eye is first refracted at the cornea. The pupil then limits the amount of light entering the eye. The lens is situated directly after the pupil, and focuses the light through the vitreous humour onto the retina at the back of the eye, forming an image. The location of the object that a relaxed eye images onto the retina is known as that eye's *far point*, which for an *emmetropic* eye will be at infinity. In order to image objects closer than the far point, muscles around the lens will contract, thickening the lens which shortens its focal length and enables the object to be imaged properly onto the retina. This is called *accommodation*.

If a relaxed eye doesn't focus light from infinity onto the retina, the eye has *refractive errors*. Refractive errors include *myopia* (near-sightedness) and *hyperopia* (far-sightedness), where the relaxed eye instead focuses parallel light to a point in front of the retina or behind the retina, respectively. Astigmatism is also considered a refractive error.

For a relaxed myopic eye, the far point is at a finite distance from the eye, and the eye is only able to accommodate for objects closer than that. Hence, objects further away than the far point will not be imaged sharply onto the retina in a myopic eye.

A hyperopic eye will instead always have to accommodate, even for objects at infinity. This can lead to eye strain and headaches. Both myopia and hyperopia can be treated with the help of corrective contact lenses or glasses.

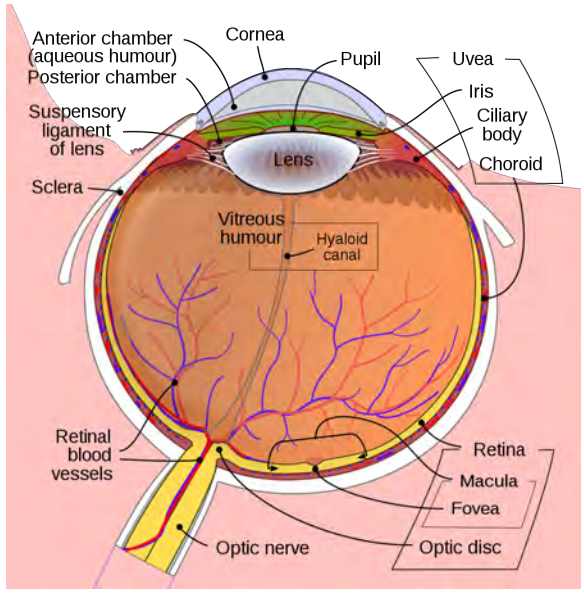

Figure 2.1: Schematic illustration of the human eye. (Image source: [3])

2.2 Aberrations

A lens (or optical system) can be subject to various *aberrations*, i.e., imperfections in the lens's ability to image an object. The larger the aberrations, the worse the image quality. Aberrations are generally divided into on-axis aberrations and off-axis aberrations. Off-axis aberrations affect only image points off the optical axis, whereas on-axis aberrations can affect all image points, both on and off the optical axis. Refractive errors are closely related to optical aberrations.

The first and often most discussed on-axis aberration in human eyes is *defocus*. Defocus means that the optical system's image plane is shifted from the desired image plane (in the eye this is the retina). This is the optical aberration of myopia and hyperopia. Like mentioned earlier, it can easily be corrected with contact lenses or glasses.

Astigmatism means that the optical system has different focal distances for rays that propagate along different planes, see Figure 2.2a. In an axially symmetrical system this is an off-axis aberration, but as eyes are rarely perfectly symmetrical, rays on the optical axis can also suffer from astigmatism. On-axis astigmatism in eyes can be corrected with non-symmetrical (cylindrical) lenses in contact lenses or glasses.

While defocus and astigmatism can be corrected with contact lenses or glasses, higher-order aberrations are not as easily corrected. Higher-order aberrations vary a lot between individuals and largely determine the vision quality once myopia,

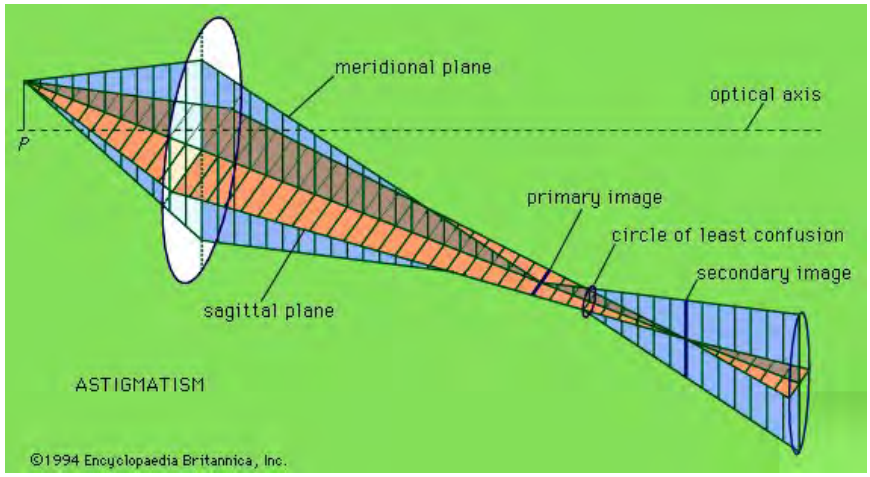

(a) Illustration of the different focii for sagittal rays versus meridional rays for off-axis astigmatism. (Image source: [4])

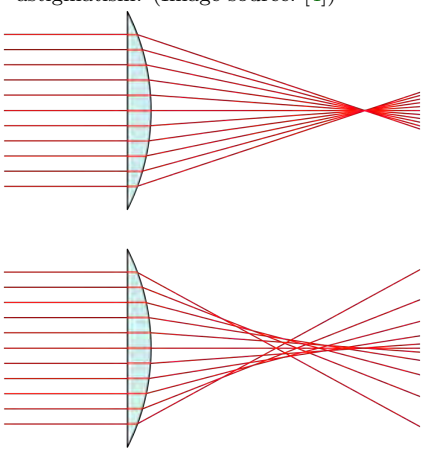

(b) Illustration comparing a perfect lens without aberrations (top) to a lens with spherical aberration (bottom). With spherical aberration parallel rays are focused onto different points depending on their radial distance from the optical axis. (Image source: [5])

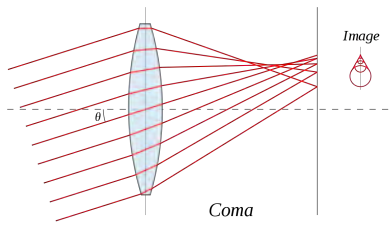

(c) Illustration of the off-axis aberration coma. The image has different magnifications depending on its rays' radial distances from the optical axis at the lens. (Image source: [6])

Figure 2.2: Illustrations of various types of optical aberrations.

hyperopia and astigmatism have been corrected.

An example of an on-axis higher-order aberration is *spherical aberration*. Spherical aberration affects all systems with spherical surfaces. Parallel rays entering the system will be focused at different distances depending on their radial distance from their optical axis. For example, for a lens with positive spherical aberration the marginal rays will be focused closer to the lens than rays close to the optical axis (see Figure 2.2b). The result is a blurry spot of what should have been a point focus.

An example of an off-axis higher-order aberration is *coma*. It causes parallel rays to focus onto the image plane at different radial distances from the optical axis (see Figure 2.2c). The image spot takes a drop/comet shape, which is how the aberration got its name. Just like for astigmatism however, coma often occurs on-axis in eyes. This is due to various asymmetries or other "imperfect" shapes in the optical elements of the eye.

2.3 Wavefront sensing

The directions of rays emerging from an optical system depend on the properties of the optical system, including the aberrations of the system. The bundle of rays thus, in essence, contain the optical information of the system it emerges from. A wavefront sensor captures this information by sensing the *wavefront* of the bundle of rays. The wavefront can be visualised as a free-form surface normal to all the rays: a parallel bundle of rays will have a perfectly flat wavefront, whereas a point source of light would give rise to a spherical wavefront. Each aberration type can be described by the way it affects a flat wavefront. Mathematically, these aberration wavefront shapes can be described by *Zernike polynomials*, which form an orthogonal base on the unit disk. A wavefront can therefore be described as a unique linear combination of Zernike polynomials. By analysing the shape of the wavefront, the coefficients for each Zernike polynomial (and thus also for each aberration) can be extracted.

Hartmann-Shack wavefront sensor

The most common type of ocular wavefront sensor is the Hartmann-Shack wavefront sensor (HSWS) [2]. The HSWS contains an array of small lenses called lenslets that focus the light in the wavefront to spots on a CCD detector placed in the focal plane of the lenslets (see Figure 2.3). If the wavefront hitting a lenslet is tilted, the dot from that lenslet will be shifted from its optical axis. Because the shift is proportional to the wavefront tilt, the shape of the total wavefront can be reconstructed from the image registered on the CCD by analysing the shifts of all the dots. The quality of the reconstructed wavefront depends on a number of factors, such as the number of lenslets, and the brightness of the spots.

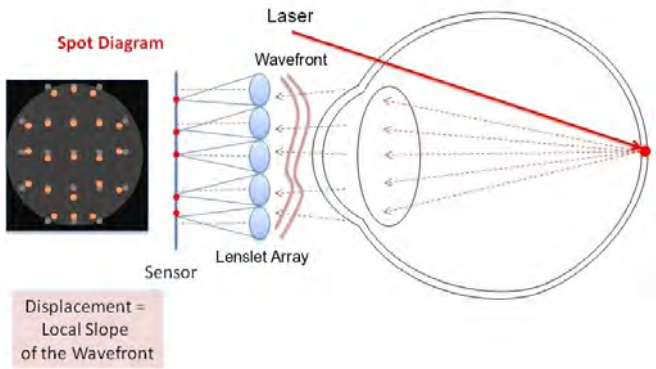

Figure 2.3: Principle of a Hartmann-Shack wavefront sensor. (Image source: [7])

Telescope

For wavefront measurements on a human eye, a weak laser is pointed into the eye which creates a dot on the retina (see Figure 2.3). This dot acts as a point source on the retina, emitting light that exits the eye. An ideal eye would give rise to a flat wavefront exiting the eye, but a real eye will not, due to the various optical aberrations in the eye. In ocular wavefront sensing, the thing we want to measure is the wavefront directly after it has passed through the optical system of the eye. This is equivalent to measuring the wavefront at the *exit pupil* of the eye, i.e. the image of the limiting aperture when looking from the image side. The limiting aperture is the eye pupil, and the image side is in this case the outside of the eye (as the object is the retinal dot). The exit pupil is thus simply the image of the eye pupil that we see when looking at the eye. As this image is located inside the eye, we need an optical system that is able to reconstruct the wavefront at the eye exit pupil onto the lenslet array of the wavefront sensor.

To reconstruct the wavefront at the exit pupil, it is not enough to only produce an *image* of the exit pupil, since an image is just a reconstruction of the ray positions at the object. What we need to do is to reconstruct both the positions *and* directions of all the rays at the exit pupil. What is needed is an optical system that has a known angular magnification and transverse magnification, so that each detected spot shift on the detector is proportional to the wavefront tilt of a part of the wavefront at the eye exit pupil. We also want this system to be as compact as possible, while still being convenient. Often the system is designed to have a transverse magnification < 1. This is because the sensor area of the HSWS is usually smaller than the eye pupil, so in order to image the entire wavefront emerging from the pupil, the wavefront needs to be made smaller.

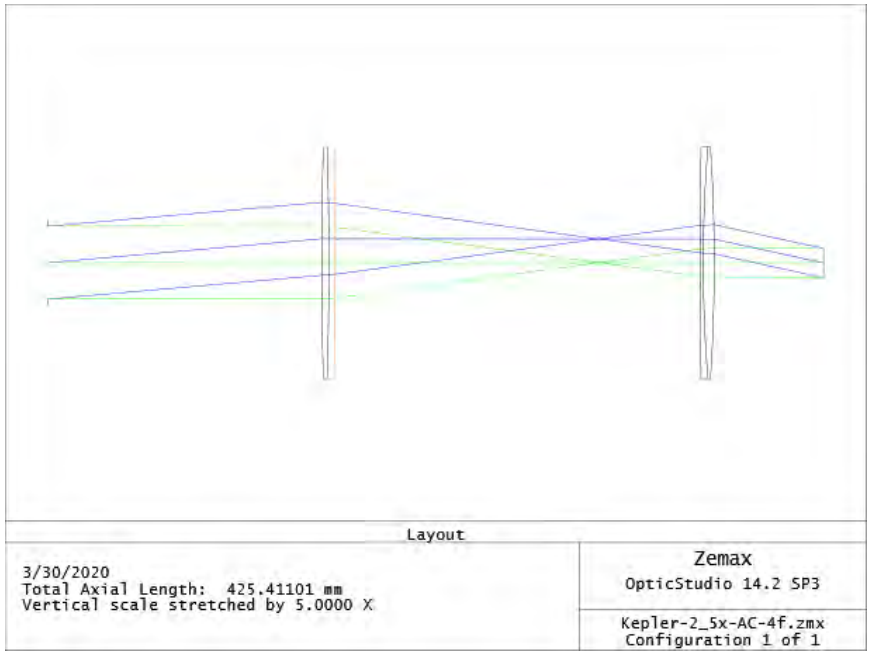

Figure 2.4: Zemax simulation of a 4f-Kepler telescope with off-the-shelf lenses from Thorlabs. The first and second lens have focal lengths $f_1 = 150$ mm and $f_2 = 60$ mm, respectively. The distance between the two lenses is $f_1 + f_2$. The object is 150 mm from the first lens and the image is 60 mm from the second lens, creating a 4f-telescope. The angular magnification is 2.5.

4f Keplerian

The most common and straightforward way to reconstruct the wavefront is with a 4f Keplerian telescope (henceforth called 4f-Kepler). In this system two lenses with focal lengths f_1 and f_2 are placed in succession at a distance of $f_1 + f_2$ from each other. The eye pupil is placed at a distance of f_1 before the first lens and the wavefront sensor is placed at a distance of f_2 after the second lens. This total length of $2f_1 + 2f_2$ is why the telescope is called a 4f-telescope. The 4f-system will produce a scaled inverted image of the eye's wavefront at the lenslet array of the wavefront sensor. [8] The angular magnification will be $-f_1/f_2$ and the transverse magnification $-f_2/f_1$. [9] An example of a 4f-Kepler system can be seen in Figure 2.4.

2f-Kepler

The 4f-telescope can be reduced in size if we choose to move the pupil and lenslet array away from the focal points of the two lenses (it will no longer be of the 4f

type). This allows us to choose shorter focal lengths for the lenses but still keep the same distance from the pupil to the first lens, see Figure 2.5. The important things are that the pupil is imaged onto the lenslet array by the telescope, that the distance between the two lenses is still $f_1 + f_2$, and that the angular magnification and transverse magnification are constant.

A calculation with ray transfer matrices show that a system like this (which will henceforth be called 2f-Kepler) will be optically identical to a 4f-Kepler telescope. Both systems have the system transformation

$$\begin{bmatrix} y' \\ \theta' \end{bmatrix} = \begin{bmatrix} -f_2/f_1 & 0 \\ 0 & -f_1/f_2 \end{bmatrix} \begin{bmatrix} y \\ \theta \end{bmatrix} \tag{2.1}$$

where y and θ are the ray height and angle at the object plane and y' and θ' are the ray height and angle at the image plane. For details, see Appendix A. From the transformation, we see that a ray at the object plane with height y and angle θ will reach the image plane at height $y' = -yf_2/f_1$ and angle $\theta' = -\theta f_1/f_2$, i.e. we have transverse magnification $-f_2/f_1$ and angular magnification $-f_1/f_2$.

The limit to reducing the size this way is that the focal length of the first lens must be larger than $s_{o1}/(M_a + 1)$, where s_{o1} is the distance between the pupil and the first lens and M_a is the angular magnification of the telescope. A complete derivation can be found in Appendix B. It is at most possible to shrink the system to half the size of the 4f-system. However, at that limit the distance between the second lens and the sensor is 0, so the practical limit is somewhat higher.

A similar but more complicated telescope design has been suggested by Sarver [10] (described in the next section), but to my knowledge a 2f-Kepler telescope has not yet been used in an ocular wavefront sensor.

Sarver

A way to make the system even more compact would be to replace the first lens with two lenses of even shorter focal length, see Figure 2.6. The choice for replacing the first lens is simply because that is the one that will usually have the longest focal length of the two in the Kepler setup. By choosing a positive first lens and a negative second lens the two lenses act together to form a system with a longer focal length than either of the two lenses separately, but which focuses the light closer to the first lens than a regular lens of the same focal length would have. The distance between the first and the last (in this case third) lens is thus decreased compared to a two-lens system and the total length of the system can be made even more compact than the 2f-Kepler system. The idea for this design in an eye wavefront sensor was proposed by Edwin Sarver [10], so here this design will be called the Sarver telescope. However, the Sarver telescope also has some practical limitations. By adding a third lens we reduce the available space inside the telescope that could be used for beam-splitters or other necessary optics that are not part of the telescope. Aligning the lenses would also be more difficult than with a Kepler telescope.

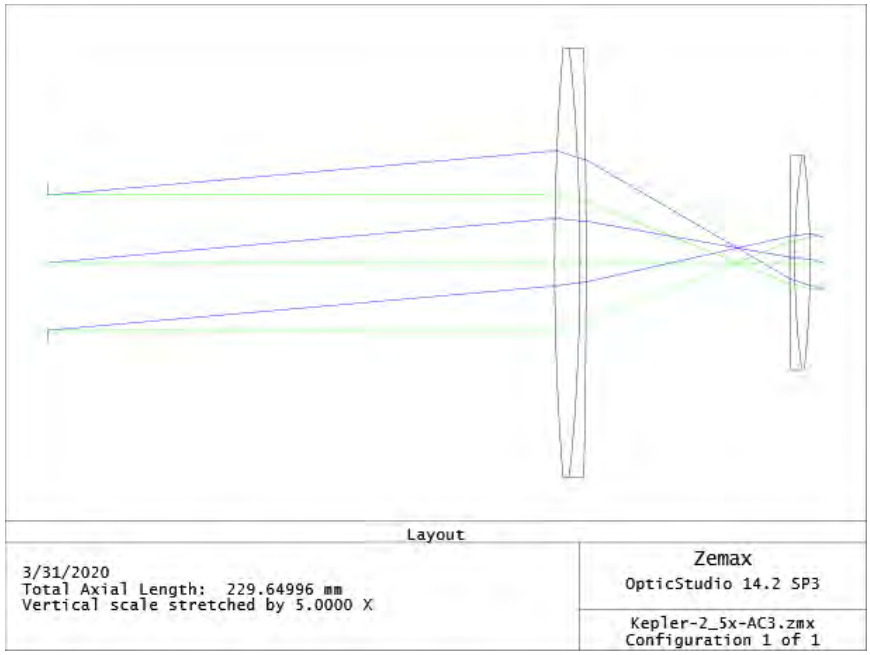

Figure 2.5: Zemax simulation of an extreme version of the 2f Kepler system. The object-image distance has almost been halved compared to the 4f Kepler system in Figure 2.4. The distance between the object and the first lens is still 150 mm, but the telescope size has been reduced by decreasing the lenses' focal lengths. The first and second lens have focal lengths $f_1 = 50$ mm and $f_2 = 19$ mm, respectively. The distance between the two lenses is $f_1 + f_2$, and the distance from the second lens to the image is only 4 mm.

Additional components

Apart from the laser, telescope and sensor a few additional components are usually used for an ocular wavefront sensor. A schematic sketch of a typical 4f-Kepler wavefront sensor can be seen in Figure 2.7. We want the person to have an open field-of-view, i.e. be able to look comfortably at different objects, without the wavefront sensor blocking the entire view. We also don't want the laser spot on the retina to be visually disturbing. By using a laser that emits infra-red (IR) light that the eye can't easily detect, the spot won't interfere with normal vision. This also enables the use of a *hot mirror*, i.e. a mirror angled at 45° that reflects IR light but is transparent to visible light. The person looks through the hot mirror, focusing on targets behind it, while the telescope and laser is placed to the side of the hot mirror, relatively out of view.

The laser beam will be partially reflected by the cornea when entering the eye. If the laser beam is centred on the eye, this reflection will interfere with the light emerging from the laser spot on the retina, disturbing the wavefront. By shifting

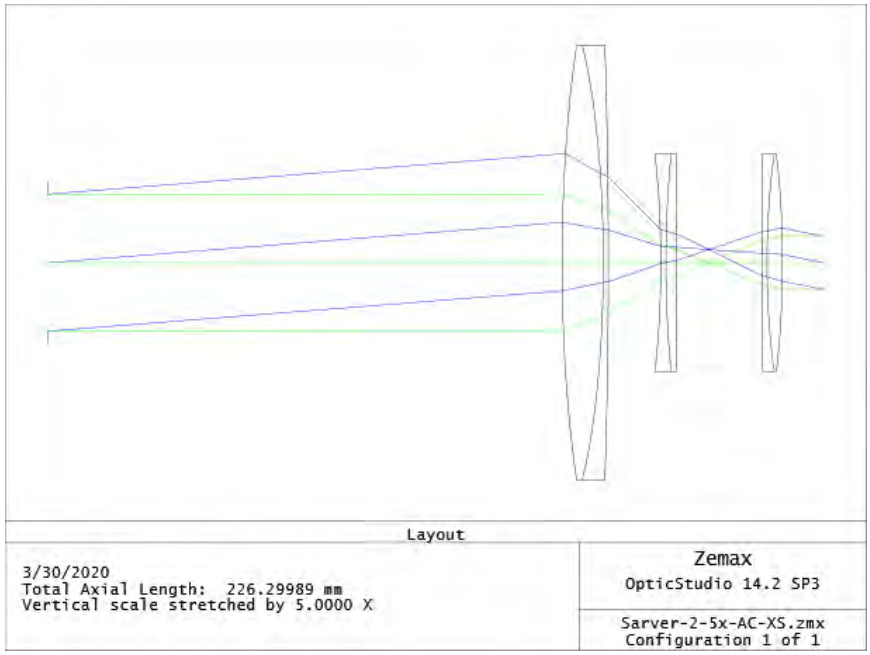

Figure 2.6: Zemax simulation of a Sarver telescope. The distance between the object and the first lens is 150 mm.

the laser beam to the side of the cornea, the reflection bounces out off the path to the telescope. This will not affect the position of the retinal spot: since the beam is still parallel to the optical axis, the beam will be focused onto the centre of the retina. Aberrations could however become more prevalent, affecting the size and shape of the retinal spot. The laser beam can be shifted with the help of a displacement window, which is a piece of glass that can be tilted, thus changing the lateral position of the laser beam.

Pupil camera

Often a pupil camera is used to ensure that the eye is properly placed in relation to the wavefront sensor. The pupil camera images the eye's pupil, and is aligned so that the eye is at the correct distance to the sensor when the image on the pupil camera is sharp. The pupil camera is thus a helpful tool to aid in the z-alignment, but it also makes the wavefront sensor larger, heavier and more expensive. For this reason, it was decided that a pupil camera would not be used. Instead, the HSWS would be used to judge if the pupil is in focus on the lenslet array or not.

Figure 2.7: A schematic sketch of a one-to-one 4f-Kepler wavefront sensor. Main components are: 1) laser, 2) beam-splitter, 3) hot mirror, 4) eye, 5) first lens (focal length f), placed f from the exit pupil of the eye, 6) second lens (focal length f, same as first lens) of telescope, placed $2f$ from the first lens, 7) lenslet array in detector, placed f from the second lens.

Chapter 3

Methods

The main design problems to solve were making the system more compact and more portable. A HASO 32-eye HSWS by Imagine Eyes was provided as detector for the setup. The rest of the wavefront sensor setup had to be compatible with the HASO sensor, while still being as compact and portable as possible.

3.1 Zemax simulations

Telescope

In order to assess the quality of the three different telescope designs, simulations were run in the optical design software *Zemax*. First, paraxial versions of the telescopes were created with off-the-shelf focal lengths to check that the correct angular and transverse magnification could be obtained. The optimal angular magnification would be 2.5, since this would allow an 8 mm wide pupil to be imaged fully (with some margins) onto the 4.5 x 3.6 mm^2 large detector [11]. The distance between the eye and the first lens was chosen to be 150 mm, as this distance would enable both a hot mirror and beam-splitter for the laser to be placed between the eye and the first lens, without the hot mirror being too close to the eye. Any larger distance than this would make the setup unnecessarily long. The reason the beam-splitter isn't placed in the middle of the telescope (where there is a lot of empty space) is that we don't want the telescope lens to destroy the collimation of the laser beam. It it also better to place it so the beam doesn't pass through the entire telescope before entering the eye, since we would risk getting reflexes of the lens surfaces that would interfere with the wavefront signal from the eye.

After confirming that all three telescope designs achieved proper wavefront reconstruction (i.e. correct angular and transverse magnification), the paraxial lenses were exchanged for models of off-the-shelf lenses from Thorlabs. This was to see if the introduction of aberrations from the lenses would change the performance of the telescope. Different telescope versions with varying magnifications and choices of focal lengths and lenses were tested, especially for the 2f-Kepler and Sarver de-

signs which had more parameters to change. The performance of the systems were assessed by comparing the spot diagrams with the airy disk of the systems: if the spot diagram was within the airy disk, the telescope was diffraction limited. It was important that the telescope is as close to diffraction limited as possible, otherwise the wavefront sensor would end up sensing not only the aberrations of the eye but of the telescope as well.

All the three telescope designs could be made on-axis diffraction limited. However, with a shorter telescope the lenses had to have shorter focal lengths, and lenses with shorter focal lengths are thicker, have higher surface curvatures and thus often have higher levels of aberrations. A way to decrease the aberrations while maintaining a short total length was to use lenses with smaller diameters. Since the telescope should reduce the size of the image compared to the object it works well to use a smaller sized lens as the second lens of the telescope.

The simulations in Zemax also showed that the Sarver system could not be made significantly smaller than the 2f-Kepler system, at least not with off-the-shelf lenses. We want to to use achromatic lenses in the telescope, both because of their low levels of aberrations, and also because they have similar focal lengths for visible light and IR light, enabling aligning with visible light but operation with IR light. Since the Sarver telescope is the most compact if the middle lens is negative, and there weren't many negative achromatic lenses to choose from, this severely limited the choice of lens for the middle lens in the Sarver telescope. All in all, the smallest Sarver design was only three millimetres shorter than the smallest 2f-Kepler design (found in Figures 2.6 and 2.5 respectively). The advantage of the Sarver design is that it can get a longer distance between the second lens and the sensor compared to a 2f-Kepler design with the same total system length. However, its disadvantage is that we limit our ability to place additional optics inside of the telescope, such as a beam-splitter or a limiting diaphragm. The simulations also showed that the Sarver design was very sensitive to misalignment. A small shift of one of the lenses made the system lose its afocality and thus its ability to properly reconstruct the wavefront.

The best compromise between system length, and adaptability and ease of alignment turned out to be of 2f-Kepler type, shown in Figure 3.1. This specific design is diffraction limited (see Figure 3.2) and is roughly 65% as long as a 4f-Kepler with the same pupil to first lens distance, measured from eye to HSWS. It uses a first lens with focal length 75 mm, and a second lens with focal length 30 mm. The main reason for choosing this design rather than an even smaller 2f-Kepler telescope is that we need some space between the second lens and the lenslet array. This is because the lenslet array in the sensor is set a bit inside the sensor casing, limiting our ability to place optics directly in front of it. The distance between the second lens and the sensor plane in this design is 17 mm, which is enough to enable proper placement of the second lens relative to the sensor lenslet array. As the second lens has a diameter of 1/2 inches, it is also small enough to actually be put inside the outer part of the sensor case. This enables it to get slightly closer to the sensor lenslet plane. Since it was difficult to measure the exact distance to the

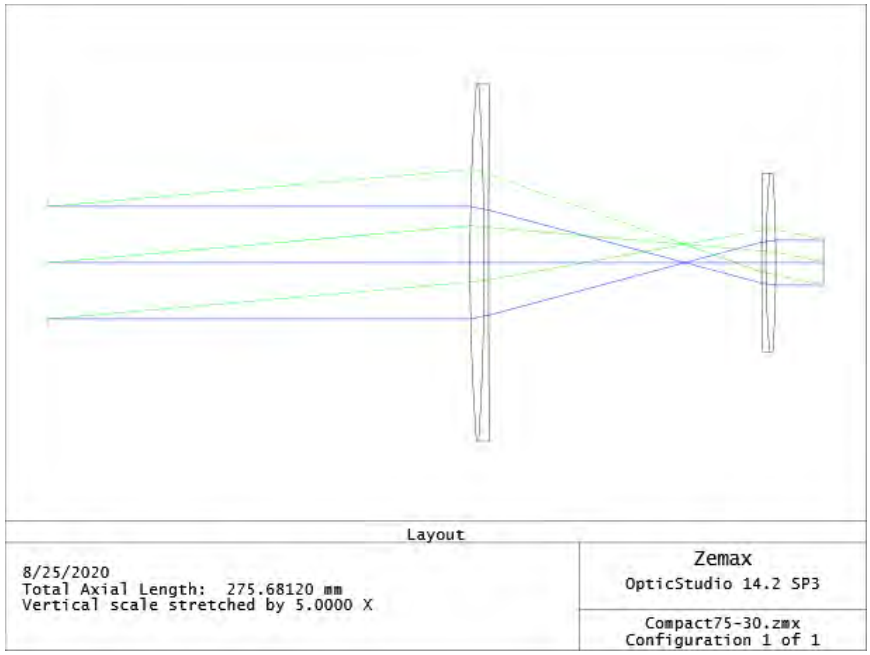

Figure 3.1: The final telescope design. The first and second have focal lengths $f_1 = 75$ mm and $f_2 = 30$ mm, respectively. The distance from the object (eye pupil) to the first lens is 150 mm. The distance from the second lens to the image (sensor plane) is 17 mm.

lenslet array from the sensor case, the telescope was designed to have second lens to lenslet array distance that is probably slightly longer than necessary.

Laser

The laser source should be an IR source that is not too visually disturbing for the eye but also has a wavelength that travel properly throughout the optical system and registers correctly on the sensor. The wavelength 830 nm has previously been used with good results for eye wavefront sensing [12], so this was chosen as the wavelength for the laser diode.

The 830 nm laser diode is connected to an optical fibre, which is then connected to a fiber-port which collimates the light emerging from the fibre tip. The choice of fiber-port affects the properties of the collimated laser beam, such as divergence and beam waist. The size of the beam waist affects the risk of getting interfering reflections off the cornea, and the divergence affects the size of the spot produced on the retina. The beam waist and divergence are also mathematically linked: the smaller the beam waist, the larger the divergence. We want a fiber-port with a

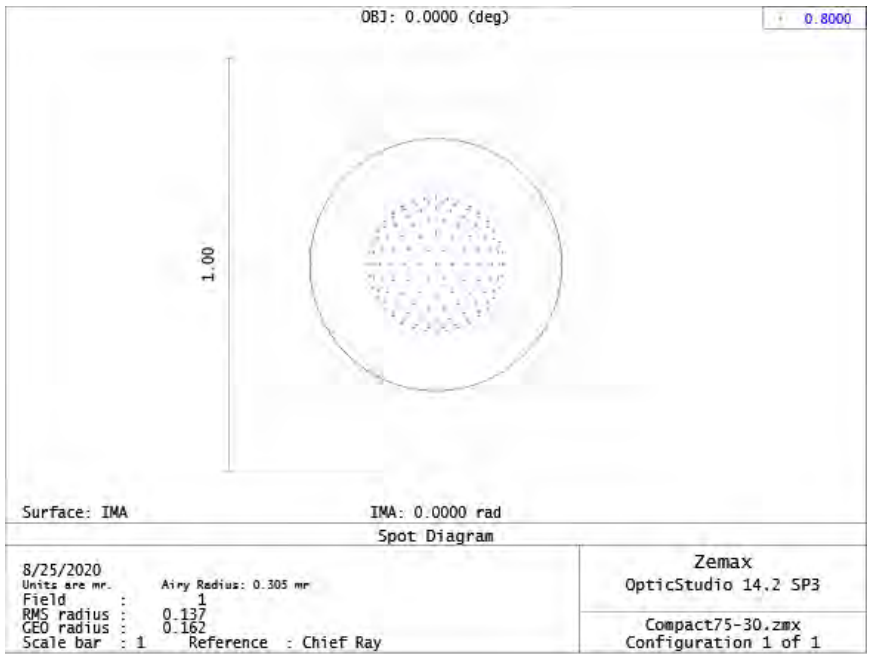

Figure 3.2: Spot diagram for the chosen telescope design. The blue dots are all enclosed within the circle of the airy disk radius, indicating that this system is on-axis diffraction limited.

good balance between beam waist size and divergence, so that both the spot size on the retina and the beam waist at the cornea are relatively small.

The properties of the laser beams from three different fiber-ports from Thorlabs were inserted into Physical Optics Propagation in Zemax. This is a mode in which you can see how a Gaussian beam would behave throughout an optical system. The laser beam was put through a lens mimicking the optics of the eye, with the beam waist placed at the lens's first surface, and the spot size on the focal plane of the lens was registered. This was performed both for a paraxial lens and for a plano-spherical lens. The results are shown in Table 3.1. The best compromise between smaller waist (to reduce corneal reflections) and small spot size seemed to be the fiber-port with part number PAF2-5B. The simulations were repeated for slight offsets both in beam waist z-position and in x-y-position. The z-offset didn't affect the registered beam size at all, but a large x-y-offset changed the shape of the spot when using a plano-spherical lens (though the registered spot size stayed the same).

Fiber-port Thorlabs	Output waist diameter	Divergence	Spot size paraxial	Spot size plano-spherical
PAF2-2B	0.43 mm	2.500 mrad	20.5 μm	22.3 μm
PAF2-5B	1.00 mm	1.087 mrad	8.81 μm	13.0 μm
PAF2-7B	1.62 mm	0.667 mrad	5.44 μm	15.6 μm

Table 3.1: Table of laser spot sizes produced on the retina for different fiber-ports.

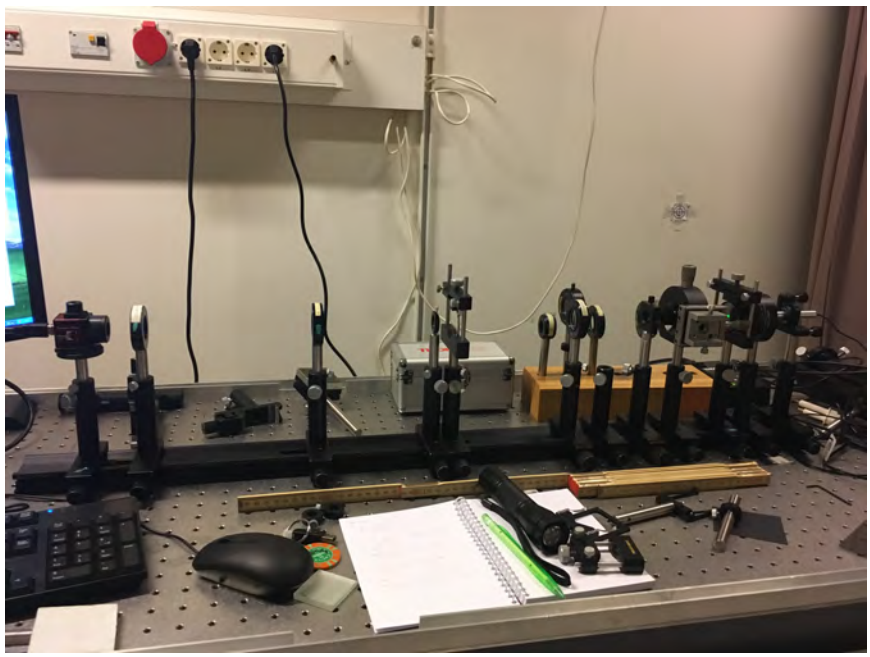

Figure 3.3: The test setup. Components from left to right: HSWS, $f = 50$ mm telescope lens, $f = 140$ mm telescope lens, aperture, trial lens mount, $f = 100$ mm collimating lens, pinhole, microscope objective, polarisation filters and laser.

3.2 Test setup

Since the simulations showed that a 2f-Kepler telescope would be the preferable telescope design, a test setup was constructed in order to compare the 2f-Kepler telescope to a traditional 4f-Kepler telescope in practice. There were two main aims with the test setup: 1) to compare the wavefront imaging properties of the 2f-Kepler with the 4f-Kepler, and 2) to compare the alignment process. The test setup was built with the components mounted directly on posts on an optical rail. An image of the test setup can be found in Figure 3.3.

A laser pointer was used as a laser source. The intensity of the laser beam was

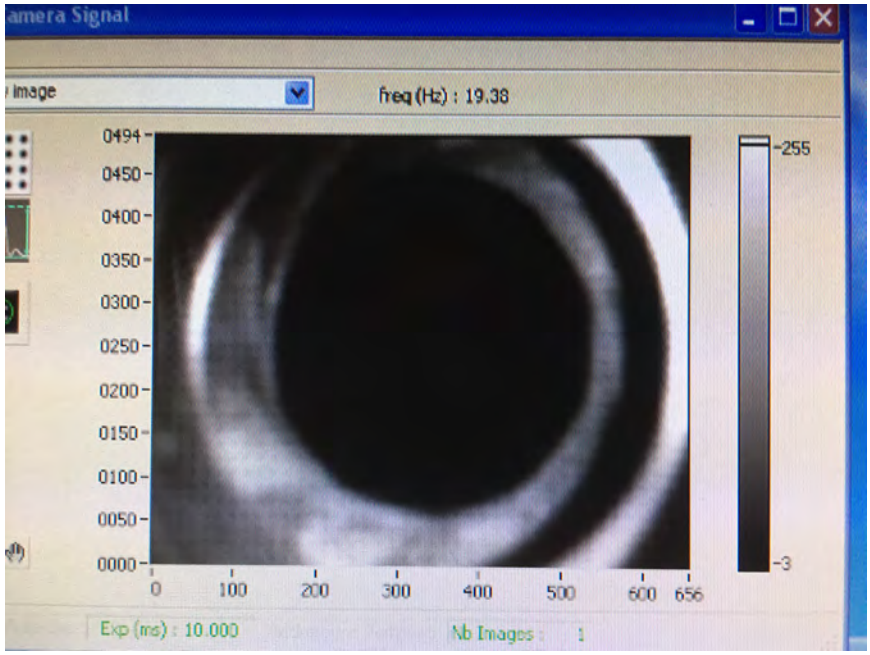

Figure 3.4: An image of the aperture has been formed on the sensor lenslet matrix, producing an detectable image. Due to the lenslet array, the image doesn't get sharper than this.

regulated by two successive polarisation filters. In order to get a clean beam the laser was focused onto a 6 μm pinhole with the help of a microscope objective. The diverging beam emerging from the pinhole was collimated with an achromatic lens with a focal length of 100 mm, which corresponds to a power of 10 diopters (D). The collimation of the emerging beam was checked with a hand-held telescope focused onto infinity. If the pinhole was in sharp focus when looking through the hand-held telescope and the collimating lens, the light exiting the collimating lens was collimated.

The collimated light then passed a mount for a trial lens and an aperture placed directly after the trial lens mount. The aperture was imaged onto the Hartmann-Shack wavefront sensor with the help of a Kepler telescope made of two achromatic lenses, the first one with a focal length of 140 mm, the second one with a focal length of 50 mm. For the 2f-Kepler telescope, this was checked by shining a torch onto the aperture and adjusting the sensor position until the image of the aperture on the sensor was the sharpest (see Figure 3.4). For the 4f-telescope, this was made by checking separately that the aperture was in the focal plane of the first lens (with the help of the hand-held telescope) and that the sensor was in the focal plane of the second lens (by removing the first lens). The afocality of the Kepler

telescopes was checked with the hand-held telescope by ensuring the pinhole was in sharp focus when looking through the hand-held telescope, the Kepler telescope and the collimating lens.

Two test runs were made with trial lenses of various powers. One test run was with a 4f-Kepler telescope, the other test run was with a 2f-Kepler telescope with the same lenses as the 4f-Kepler. First, a reference wavefront without a trial lens was saved. Then a trial lens was inserted at the aperture, and two files with aberration values were saved: one with the "raw" data, and one which had been compensated by removing shifts from the reference file. The registered pupil size was also recorded. Both positive, negative and cylindrical trial lenses were used, and their orientation was noted so that they were oriented the same way when test runs were made with the other Kepler telescope setup.

The analysis consisted of comparing the registered Zernike coefficients for defocus, spherical aberration, astigmatism and coma between the two test runs, i.e. between the setup with the 4f-Kepler telescope and the one with a 2f-Kepler telescope. If the registered values were the same, we could be certain that the 2f-Kepler can replace a 4f-Kepler system. The values of the Zernike coefficients were adjusted to correspond to the same pupil size.

The Bland-Altmann plot in Figure 3.5a shows the difference in defocus values for the 2f-Kepler and 4f-Kepler setups. The measured values are similar, but there is some variation between the 4f-setup and the 2f-setup. For other aberrations, like spherical aberration, we see that there is a systematic error in the run with the reference wavefront removed, see Figure 3.5b. The same systematic error for the runs with removed reference wavefront appears for other Zernike coefficients as well, indicating some error with the reference files. Usually, we would have expected the opposite, since the purpose of the reference file is to enable us to remove systematic differences.

It also turned out that the image of the aperture actually was not exactly on the lenslet array in either the 4f-Kepler or 2f-Kepler setup. This could be seen by looking at the registered aperture size on the sensor. If the image of the aperture had fallen exactly onto the lenslet array the aperture size should have stayed the same, regardless of what trial lens was put behind it. However, for both telescopes the registered aperture size got larger with positive trial lenses and smaller with negative trial lenses, indicating that the aperture was not positioned correctly. It is possible that this slight misalignment of the system could also be responsible for the systematic errors we see between the two test runs. This property could possibly also be used as a tool to make sure that the aperture and sensor are properly aligned.

Since the differences between the two Kepler designs were small, it was decided that the 2f-Kepler design should be the telescope design used for the final setup.

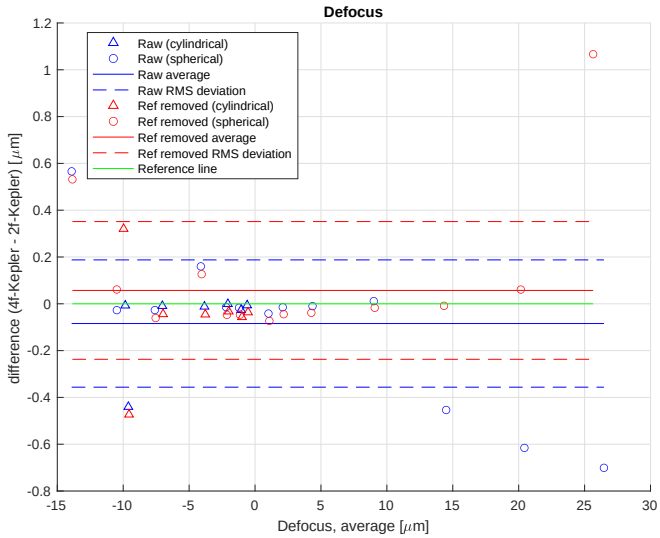

(a) Bland-Altmann plot of the defocus Zernike coefficients in the test runs.

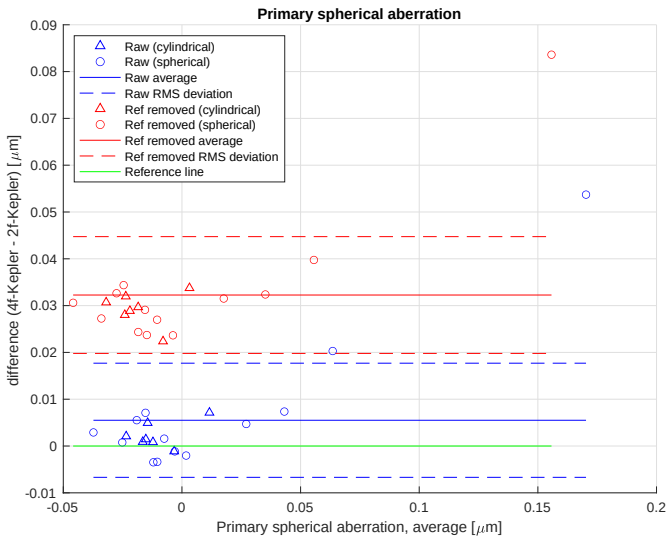

(b) Bland-Altmann plot of spherical aberration Zernike coefficients for the various trial lenses in the test setup.

Figure 3.5: Each circle and triangle represents a spherical or cylindrical trial lens, respectively. The x-axis shows the average measured aberration between the 4f-Kepler and 2f-Kepler setup, and the y-axis shows the difference between the two measurements. The blue colour indicates the test runs without any removed reference wavefront, and the red colour indicates the test runs where the reference wavefront have been subtracted from the measured wavefront. The green line is a reference line, showing where the ideal line where all lenses would lie if there was no difference between the measurements from the 2f-Kepler and 4f-Kepler setups. The dotted lines show the RMS deviation from the average.

3.3 Final setup

From the simulations and confirmation by the test setup, a 2f-Kepler telescope with the lenses described at the end of section 3.1, namely a 1 inch diameter $f = 75$ mm achromat and a 1/2 inch diameter $f = 30$ mm achromat were used.

Optomechanics

The optomechanics, i.e. the additional components connected to the optical parts, also play a big part in whether the final system is compact and portable. The idea was to have every optical component connected as a single unit. This would make the system much easier to move, because there wouldn't be a need to re-align the optics after moving the system.

The best way to do this was by using a cage system. It consists of four parallel metal rods that the optical components can be fastened between with the help of cage plates or cage cubes. The rods thus connect the optical components directly to each other and ensures they are aligned in the x-y-direction, while allowing translation in the z-direction. The whole cage system can then be mounted on an optical rail or an optical table. If all the optical components are connected together with a cage system, moving the wavefront sensor would simply be a matter of dismounting the cage system and re-mounting it somewhere else.

There are three sizes of cage systems available from Thorlabs: 16 mm, 30 mm and 60 mm. The size indicates the centre-to-centre distance between two adjacent rods. The 16 mm cage system would limit the field-of-view through the hot mirror too much, and the 60 mm cage system would be unnecessarily large and bulky. The 30 mm cage system enables large enough optical components while still maintaining a compact and portable size. The preferred lenses for the 2f-Kepler telescope were compatible with the 30 mm cage system. The second lens fits within a 1/2 inch lens tube which can be inserted into the aperture of the sensor.

Sensor mounting

The main problem to solve was how to fit the sensor to the assembly. The sensor to be used in the setup is manufactured by Imagine Eyes and doesn't fit with any of the standard mounts from Thorlabs. The sensor casing is a 30x35x32 box with a 12.7 mm long circular aperture in front with an outer diameter of 30 mm. The entire box thus does not fit within the 30 mm cage system.

The following four alternatives for sensor mounting were considered:

1. **Customise a 30 mm blank cage plate**
   A blank cage plate is simply a metal cage plate with holes for rods but no pre-made mounting holes for optics. The idea was to drill a 30 mm wide hole in the centre, through which the aperture of the sensor could be inserted and fastened. The aperture fits between the rods, though the rest of the sensor

case does not, so the rods would have to end at the cage plate. This design is very simple and compact, but there isn't room for much adjustments in the sensor position and tilt.

2. **Customise a 30 mm kinematic mount**
   Similar to the first option, but instead of customising a plain blank cage plate we would customise a kinematic tip/tilt mount. The aperture of the sensor would be fastened to the kinematic part of the mount, enabling it to be tipped and tilted if needed. However, the kinematic plate of the mount is held up by springs, so even if the sensor was aligned perfectly it would probably not be after a while when the springs lengthen.

3. **Build a platform inside a 60 mm cage system**
   If we want even more adjustment possibilities than tip/tilt we need to mount the sensor from beneath on an adjustable mirror platform. However, this option turned out to be much more complicated than it might seem at first. In order to achieve this with pre-made parts from Thorlabs, the 30 mm cage system of the telescope would have to be connected to a vertical 60 mm cage system containing the sensor and sensor mounting. The 60 mm cage in turn contains a 30 mm cage system, that would have to be rotated by 45 degrees in order for the adjustable mirror platform for the sensor to fit between the 60 mm cage rods. It becomes both large, heavy and expensive, and the many adjusting options may actually make the system less rigid, so the fine adjustments possibilities may actually not be useful due to the inherent instability of the construction.

4. **Mount the sensor separately from the cage system**
   Not desirable, but a last option if none of the other options work. The sensor would be mounted separately on the optical table/optical rail that the cage system is also mounted on. It is stable and regular adjusting techniques can be used for the sensor. However, this makes the system much less portable.

The third option was deemed to large, expensive and unstable. The first option was the smallest design and it would also be more stable than the second option, hence that one was chosen. The only worry was whether the inability to fine-adjust the position and tilt of the sensor would be a problem. In order to give us some level of adjustment abilities, two blank cage plates were ordered. In case the drilled hole in the first cage plate was slightly misplaced, the second cage plate could be used instead with a new hole slightly adjusted. As long as the entire pupil can be imaged onto the lenslet array, the lateral displacement of the sensor shouldn't matter.

Final design

A CAD drawing of the final design was created to help judge how all parts would fit together. The drawing can be found in Figure 3.6. The beam-splitter is the

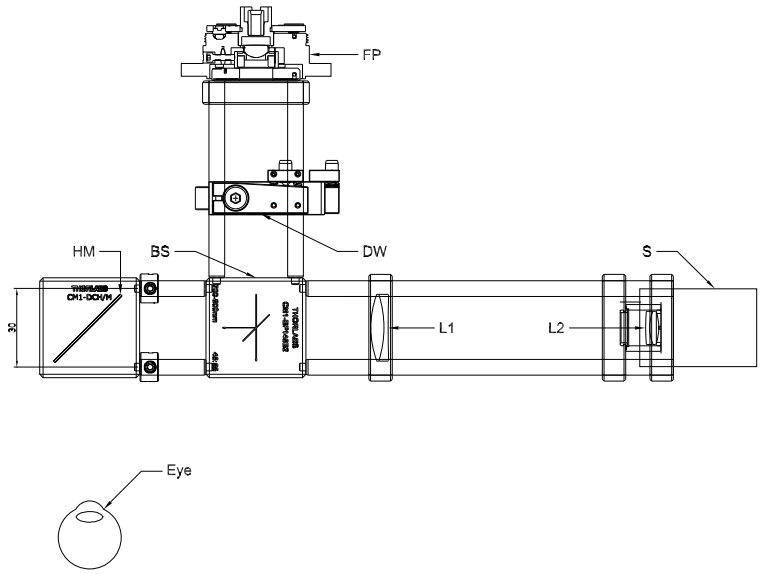

Figure 3.6: Top view of the final design. Main components are HM) hot mirror placed at 45°, BS) pellicle beam-splitter, L1) 75 mm achromat, L2) 30 mm achromat, S) HASO 32 - eye Hartmann-Shack wavefront sensor, DW) displacement window for laser beam, inside gimbal mount, FP) fiber-port connected to the laser diode.

central component, connected to the hot mirror, fiber-port and telescope by three sets of cage rods. The bottom of the beam-splitter is mounted to an optical rail by a mounting post. The blank cage plate holding the sensor is also mounted to the optical rail. The extra rods between the beam-splitter and hot mirror ensure that the laser side-cage doesn't block the field-of-view through the hot mirror more than necessary. A list of the components used in the final setup can be found in Table C.1 in Appendix C.

Construction

The telescope rods were shortened from 152.4 mm to 140 mm, and a 30 mm wide hole was drilled in the blank cage plate. Three M4-threaded holes were also made through the sides of the cage plate into the centre hole. The sensor could then be placed in the hole of the cage plate and fastened with three M4 screws.

The system alignment process can be divided into four main parts, each with individual steps:

1. Aligning the reference light

    a) The HeNe laser was added to the optical rail. A screen with marked centre was then placed directly after the laser. The screen functioned as our movable reference that enabled centring of all optical components at a common optical axis. The front part of the laser was then adjusted so that the laser beam hit the screen centre.

    b) The screen was moved to the far end of the rail. The tilt of the laser beam was then adjusted with the screws at the back of the laser mount until the beam once again hit the centre of the screen.

    c) Polarising filters were added after the laser to limit beam intensity.

    d) A microscope objective was added after the polarising filters and aligned with the screen.

    e) A filtering 6 μm pinhole was added after the microscope objective in a translation mount. The pinhole was then aligned so that the microscope objective focused the laser beam onto the pinhole. The better the focus, the brighter the beam emerging from after the pinhole. When the pinhole was correctly aligned, a bright airy disk could be seen after the pinhole.

    f) A collimating achromatic lens was added after the pinhole. It was first aligned vertically with the help of the screen. It was then aligned in the z-direction so that it properly collimated the light from the pinhole. The collimation was checked with a shear plate, a hand-held telescope and the HSWS.

2. Initial alignment of the IR laser

    a) The beam-splitter was mounted on the optical rail and the rods for the telescope was attached. The cage system was oriented so that the telescope rods were parallel to the optical rail.

    b) The first lens was added to its cage plate and mounted on the telescope rods. The lens focused the collimated light onto a spot, which enabled adjustment of the height of the cage system till it was aligned with the optical axis.

    c) Perpendicular rods for the IR laser were added and the cage system was rotated 90 degrees so the IR laser rods were parallel to the optical rail. The gimbal mount with displacement window was added to the rods.

    d) The reference laser was used to adjust the displacement window so it was normal to the optical axis. This was done by looking at where the reflections off the window ended up. The gimbal mount was locked in this position for the rest of the alignment.

    e) The fiber-port was added to the rods and connected to the laser diode. The screen was used to adjust the fiber-port so the laser beam was centred and reasonably collimated.

3. Aligning the telescope and sensor

    a) The cage system was rotated back 90 degrees so the telescope rods were once again aligned with the reference laser's optical axis. The first lens was used to double-check the alignment.

    b) The second lens and sensor were added to the end of the rods. The sensor was fixed to the far end of the rods, and the second lens was put as close to the sensor as possible. The second lens was then also fixed to the rods.

    c) The telescope was aligned to afocality by moving the first lens along the rods while checking the level of defocus registered by the HSWS.

    d) The aperture was placed at the conjugate plane of the lenslet array. This was checked by shining a torch onto the aperture and adjusting its z-position till its image onto the detector became sharp.[1] The distance between the aperture and hot mirror cube was 4 centimetres. As this was the distance that was aimed for (good field-of-view, but not uncomfortably close to the hot mirror), no adjustment of the telescope position relative to the HSWS was necessary.

    e) Reference wavefront measurement were taken with the reference light. Several wavefronts were saved, with and without aperture and also with and without averaging over multiple measurements.

4. Hot mirror and final adjustments

    a) The hot mirror was mounted in its cage cube and connected with rods and rod adapters to the beam-splitter. A second optical rail was then added underneath the hot mirror, perpendicular to the main rail. A screen was placed on the the second optical rail.

    b) The fiber-port was adjusted so that the IR laser beam was parallel to the second rail and its beam waist at the pupil plane. Once the fiber-port was aligned, the gimbal mount was loosened so it could be used to shift the laser beam for measurements on eyes.

In addition to the components mentioned above, a diaphragm was 3D-printed to be put at the common focal point of the telescope lenses. The diaphragm had a centred hole with a diameter of 3 mm, which is the size of the beam that an 8 mm pupil from an eye with a refractive error of $+5$ D or -5 D would give at the common focal point. The diaphragm worked satisfactorily to limit stray light into the sensor. However, a natural side-effect of this was that it also limited the amount of light that could reach the sensor during positioning of the eye. For this reason, the diaphragm was not used.

[1] It was later discovered that this method did not work to find the correct position for the aperture, see the discussion in Chapter 4.1.

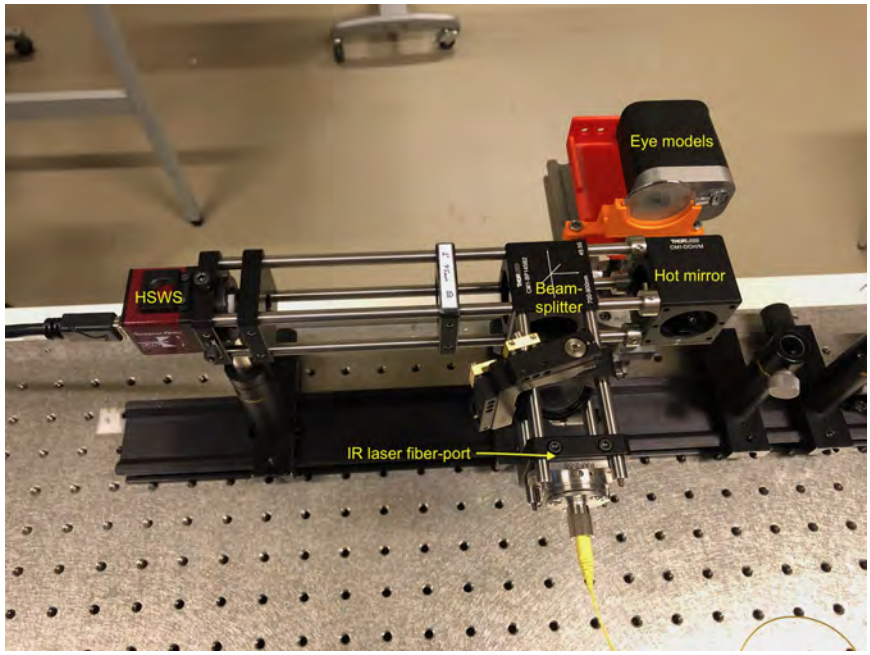

Figure 3.7: The final setup along with the eye models and a trial lens placed in front of the eye model.

During the construction it was discovered that the hot mirror ordered was a red hot mirror, i.e. a hot mirror that mainly reflects red light rather than IR light. According to the specifications however, the reflectivity of the mirror was 74% at $\lambda = 830$ nm, which was deemed high enough for our purposes.

3.4 Evaluation tests

Several experiments were performed in order to evaluate the final setup.

Eye models

These experiments were performed on two eye models with refractive errors of $+5$ D and -5 D (hyperopic and myopic, respectively), situated inside a common casing with separate apertures. The sign of the refractive error for eyes is the sign of the lens that would correct the refractive error of the eye. The eye models were mounted onto the second rail, see Figure 3.7.

Trial lenses: sharpest image

The aim of this experiment was to measure on two eye models and check if the calculated mean power from the measured wavefronts corresponded to the known refractive errors of the eye models. Trial lenses were also placed in front of the eye models to check if the correct values were obtained for various levels of defocus.

Each eye model was measured first without any trial lens, and then with various trial lenses that, to different degrees, corrected for the refractive errors of the eye model. The Zernike coefficients and pupil size were recorded for a few seconds in each measurement, with the reference wavefront from the telescope alignment (see list number 3e on page 25) subtracted from the measured wavefront. The reference wavefront chosen was the one without an aperture and with an averaging over 10 measurements. The eye model labelled 'Tool#1' had a refractive error of +5 D, so trial lenses of powers 1 D, 2 D, 3 D, 4 D and 5 D were used for that model. Similarly, the eye model labelled 'Tool#2' had a refractive error of −5 D, so trial lenses of powers −1 D, −2 D, −3 D, −4 D and −5 D were used. Additionally, cylindrical lenses with cylindrical powers −1 D and −2 D were used for Tool#2. Each measurement was repeated three times, and for each repetition the eye model was re-positioned so that the image of it was as sharp as possible on the sensor. This was checked by

1. letting the IR-laser produce a spot on the eye model case, and adjusting the eye models' z-position to minimise the imaged laser spot (see Figure 3.8b), and

2. shining a torch on the eye model case and adjusting the z-position till the image on the sensor was as sharp as possible (see Figure 3.8a).

Though there was a z-position interval of a few millimetres in which the image had roughly the same sharpness, the two methods agreed with each other for the 'correct' position of the eye models. However, the two eye models had significantly different detected pupil sizes, indicating that they were off in the z-direction. For this reason, the second experiment with trial lenses were performed, where the eye models were instead placed so their detected pupil sizes were equal.

Trial lenses: equal pupils

This experiment was identical to the first experiment except for a few details. In this experiment the eye models were instead positioned so that their detected pupil sizes were equal. This was roughly two centimetres further away from the telescope than in the first experiment. At this z-position the eye models were clearly out of focus on the HSWS, see Figure 3.9. The apertures were 5 mm in diameter, which after de-magnification by the telescope would be 2 mm. Since the HSWS only has a pupil size precision of roughly 50 microns, the detected pupil sizes switched between

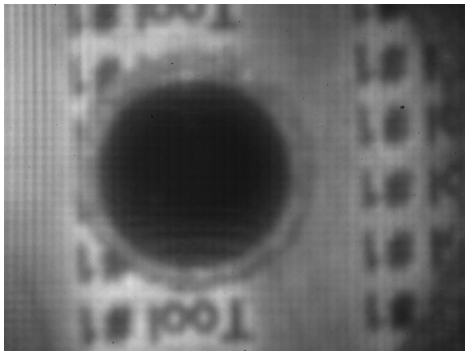

(a) HSWS sensor image of the aperture of Tool#1 when illuminated by a torch. The text around the aperture can be read.

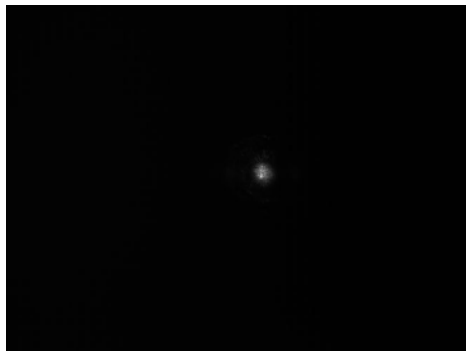

(b) HSWS sensor image of an IR spot on the eye model case.

Figure 3.8: Camera images from the HSWS with the eye models placed for best image sharpness.

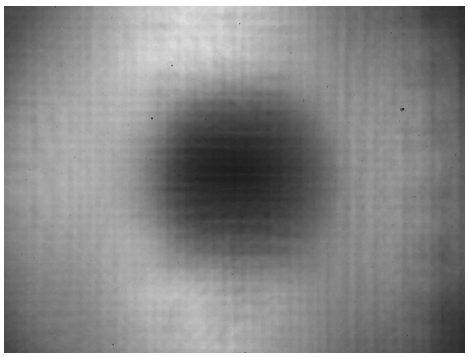

(a) HSWS sensor image of the aperture of Tool#1 when illuminated by a torch. The aperture is clearly out of focus.

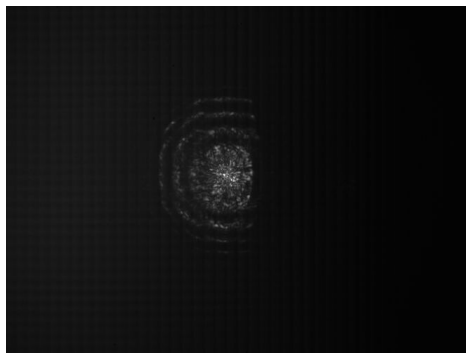

(b) HSWS sensor image of an IR spot on the eye model case. Multiple stretched out lenslet spots can be seen.

Figure 3.9: Camera images from the HSWS with the eye models placed so their detected pupil sizes were equal.

1.969 and 2.024 mm for both of the eye models, giving us some uncertainty for the z-position.

Once the eye models had been positioned so that they had similar pupil sizes their z-position was not changed. Thus only one repetition was made for each trial lens.

Z-variation

The aim of this experiment was to check how the detected refractive error of the eye models (without trial lenses) changed with z-position. The eye models were put as close to the hot mirror as possible, limited by the intersection of the optical rails. The Zernike coefficients and pupil sizes of the two eye models were then recorded in intervals of 5 mm in z-position, up till the eye models were 35 mm away from the initial position. The sharpest image and equal pupil sizes (the z-positions for the two experiments above) were at roughly 10 mm and 25 mm, respectively.

Dual-angle comparison

In addition to the experiments above a single measurement on the eye models with another wavefront sensor at KTH was performed. This other system is the dual-angle system described in [12]. This allowed comparison of the measurements from the two systems. The eye model Tool#2 was put in focus with the pupil camera of the dual-angle system and the Zernike coefficient for defocus (C_2^0) was recorded, along with the pupil size. The eye model was then moved to the compact wavefront sensor, placed so the image of it was sharp on the HSWS, and the pupil size and Zernike coefficient for defocus were recorded.

Human eye

After the eye model tests had been performed and analysed, a few measurements were also performed on three test subjects to test how the setup worked in practice. The tests followed the Declaration of Helsinki. [13]

As the results from the eye model tests suggested that a pupil camera was needed (see Chapter 4.1 for details), the pupil camera from the dual-angle system was moved and placed behind the hot mirror of the final setup and focused to the correct distance. The second rail was used as a primitive head rest for the test subjects. An IR lamp was also moved from the dual-angle system and placed next to the second rail, used to illuminate the eye for alignment with the pupil camera, without discomfort for the test subject.

Before each subject was measured on, the power of the laser beam from the hot mirror was measured with a power meter. The power was just below 30 μW for all measurements, which is below the maximum allowed value of 70 μW for continuous exposure [14].

The test subject was asked to place their hand on the optical rail and rest their chin on their hands. The IR lamp was shone onto their right eye and they were asked to adjust their head position so that the image of the pupil of the right eye was in focus on the pupil camera. The IR lamp was removed and the IR laser turned on. Fine-adjustments in the x and y directions were then needed to centre the pupil on the HSWS. For some of the measurements there were problems with IR reflections from other parts of the setup, see Figure 3.10. For instance, the beam transmitted straight through the beam-splitter passed just beside the right

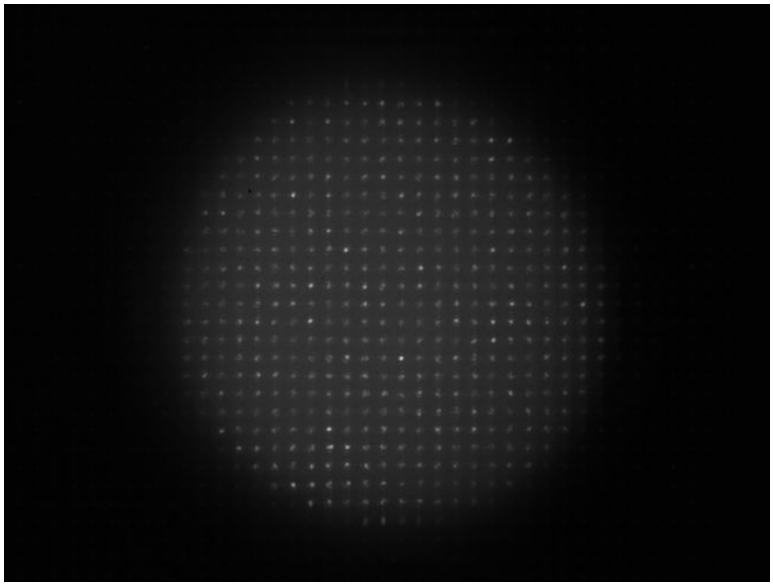

(a) A wavefront from a human eye imaged onto the HSWS. The pupil is centred on the sensor area and no extra reflections are seen.

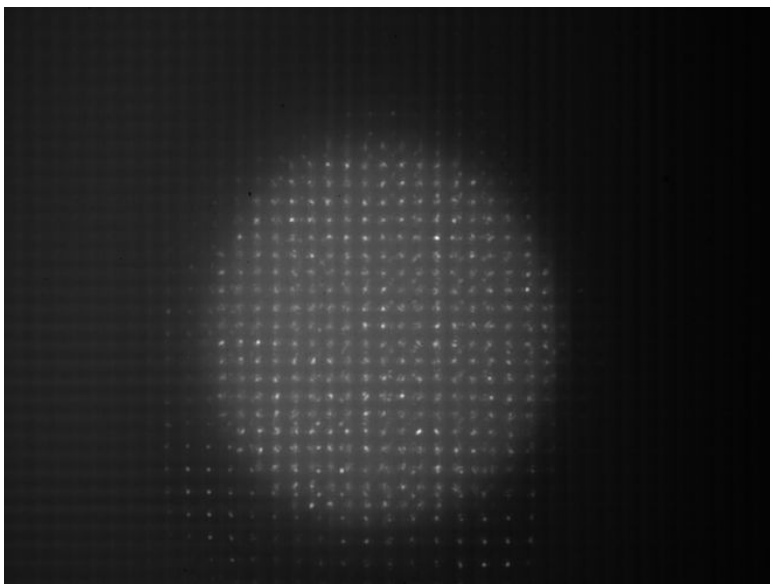

(b) HSWS image of a wavefront from a different test subject. An interfering spot pattern can be seen as well as the spots from the test subject's eye.

Figure 3.10: HSWS images from measurements on two test subjects.

ear, and any hair or skin that was caught in the beam reflected unwanted light back to the sensor. For this reason there was sometimes a need to ask the subject to tilt their head a certain way so that the beam could pass uninterrupted beside the head. However, as the eye was still aligned the same, this did not affect the measurements.

For two of the test subjects, measurements were only taken on the fovea. For the third test subject, an additional measurement in the periphery was also taken, to check that we registered the correct sign in the Zernike coefficients for coma.

Chapter 4

Results and discussion

Interpreting the results from the experiments on the final setup was an iterative process where results from the different experiments helped explain results in each other. For this reason, this chapter will not cover each experiment separately, but rather discuss this iterative process untangling the results from the multiple experiments.

4.1 Eye model tests

The mean spherical equivalent refractive errors of the eye models were calculated with the equation for Zernike defocus [15, 16]:

$$M = -\frac{4\sqrt{3}C_2^0}{r^2}, \tag{4.1}$$

where r is the pupil radius and C_2^0 is the normalised Zernike coefficient for defocus according to ANSI standard Z80.28-2004 [17]. The negative sign is because the signs for refractive errors of the eye corresponds to the sign of the lens you would need to correct the refractive error.

Graphs displaying the measured powers and pupil sizes for the test with trial lenses can be found in Figures 4.1a and 4.2a. It is apparent that we have a systematic error between measured power and expected power, both for the test where the eye models were put in focus and the test where the eye models were placed so they had the same pupil size. However, the refractive error for Tool#2 was -4.2 D for the compact system, and -4.3 D for the dual-angle system, so the two systems seem to give similar results.

We also note that the measured power was not linear for the experiment 'Trial lenses: sharpest image', as can be seen in Figure 4.1a. The pupil size also varied significantly between the eye models in this test, see Figure 4.1b. However, for 'Trial lenses: equal pupils' the measured power was approximately linear, see Figure 4.2a. The pupil size varied slightly even for these tests (see Figure 4.2b), but this variation

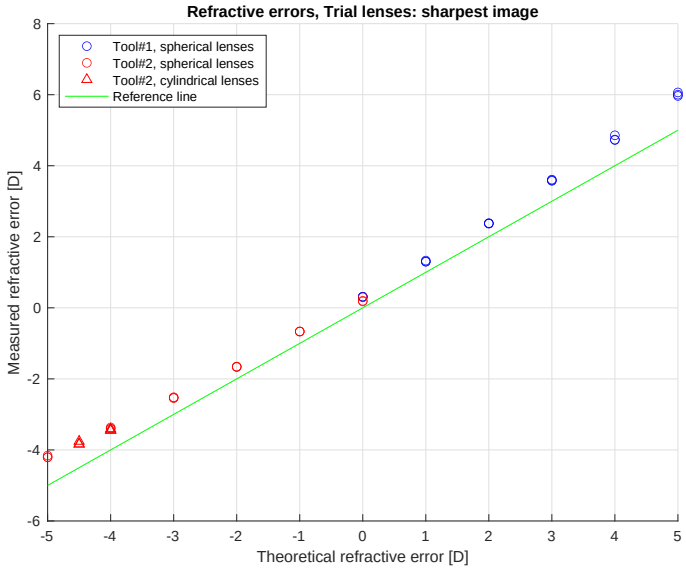

(a) Measured vs. theoretical refractive error. The theoretical refractive error is the refractive error of the eye model - the power of the trial lens used. We see both a systematic error from the reference line and a bend in the curve for the measurements.

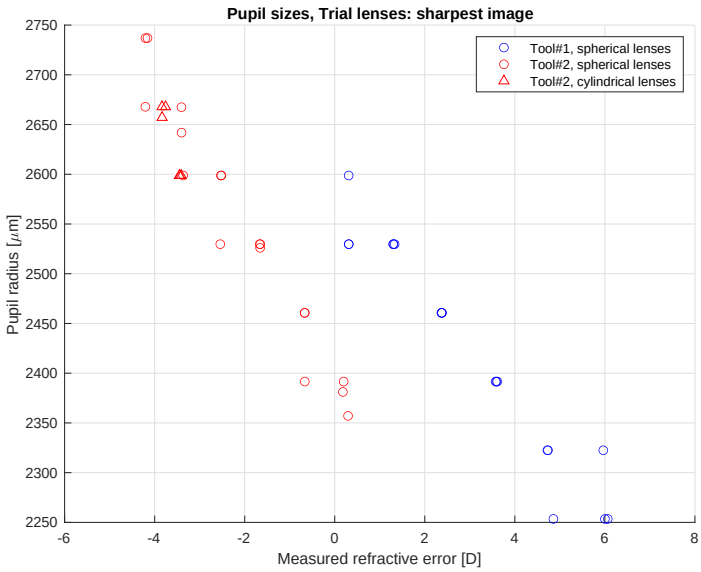

(b) Pupil radius (in the object plane) vs. the measured refractive error. There is quite a large variation in pupil sizes, that is not explained solely by the magnification of the trial lenses.

Figure 4.1: Measurements from the first experiment (Trial lenses: sharpest image).

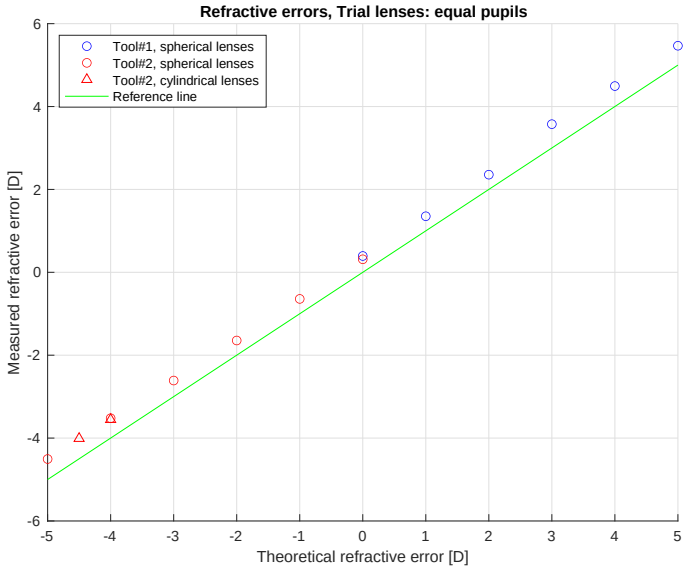

(a) Measured vs. theoretical refractive error. The theoretical refractive error is the refractive error of the eye model - the power of the trial lens used. We see a systematic error from the reference line.

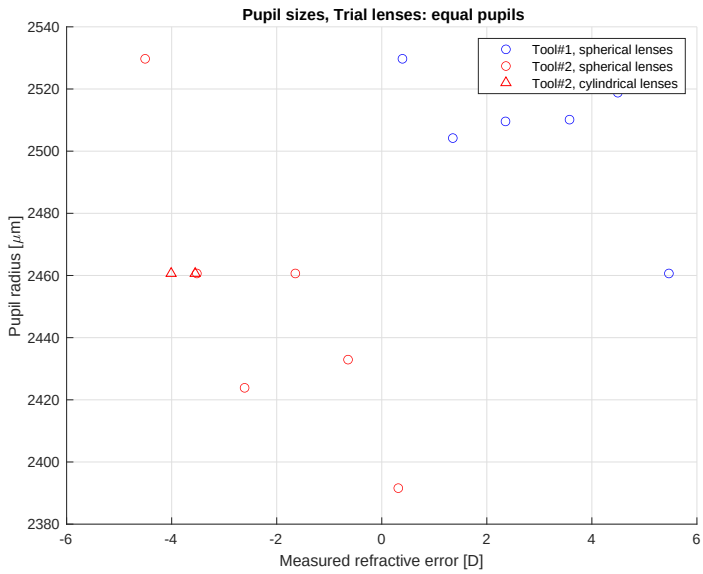

(b) Pupil radius (in the object plane) vs. the measured refractive error. The variation seen in pupil size is quite small and can be expected from the magnification of the trial lenses.

Figure 4.2: Measurements from the second experiment (Trial lenses: equal pupils).

is expected because the trial lenses slightly change the apparent pupil size of the eye models.

Wavelength correction

The systematic error in measured power can be explained by the dispersion of the eye models and trial lenses. If the eye models have a refractive errors of +5 D and −5 D at $\lambda = 550$ nm (ANSI standard wavelength for reporting eye refractive errors [17]), the measured power will be different at other wavelength. This difference can be corrected for, if you know the dispersion of the material.

However, if we correct the measurements to 550 nm with the dispersion of the human eye, we've actually over-corrected for the systematic error. Correcting with the dispersion for glass BK7 (a standard glass type often used in optical components) gives similar results as when correcting with the dispersion of the eye.

The results from the Z-variation also indicate that something is off with the wavelength correction or with the eye models. With wavelength correction down to 550 nm we can almost get the correct values for the refractive errors of the eye models, but the z-position that gives the correct value differs between Tool#1 and Tool#2, see Figure 4.3. For this wavelength correction the difference between correct position is > 15 mm. However, as the wavelength correction mainly shifts the graph up or down, and the slopes for the two eye models are different, there ought to be a wavelength for which the two graphs cross +5 D/−5 D at the same z-position. Indeed, for a wavelength correction to 675 nm, the two eye models' correct z-positions coincide at 30.5 mm, see Figure 4.4. This suggests that we should use wavelength correction to 675 nm for the two trial lens experiments.

Unfortunately, as the specifications of the eye models are unknown, we can't check at which wavelength they were supposed to have ±5 D refractive error or what they are made of. Had we known that, we could have used a correct dispersion model for that material, and checked that we got a correct value for the power of the eyes models with that wavelength correction.

Z-position

Though the wavelength correction reduces the systematic error, we still don't have linearity in the measured power for the first experiment (Trial lenses: sharpest image). This fact together with the large variation in pupil size for that experiment lead to the conclusion that the eye models were most likely not put in the correct z-position. The second experiment (Trial lenses: equal pupils) yielded a much more linear response. However, for this z-position, the eye models were clearly out of focus on the sensor. An explanation for these discrepancies would be that the assumption that the sharpest image is when the pupil image falls on the lenslet array is wrong.

The easiest way to check this is by simulation in Zemax. According to the data sheet for the HASO 32-eye HSWS the distance between the lenslets is 114 μm, but

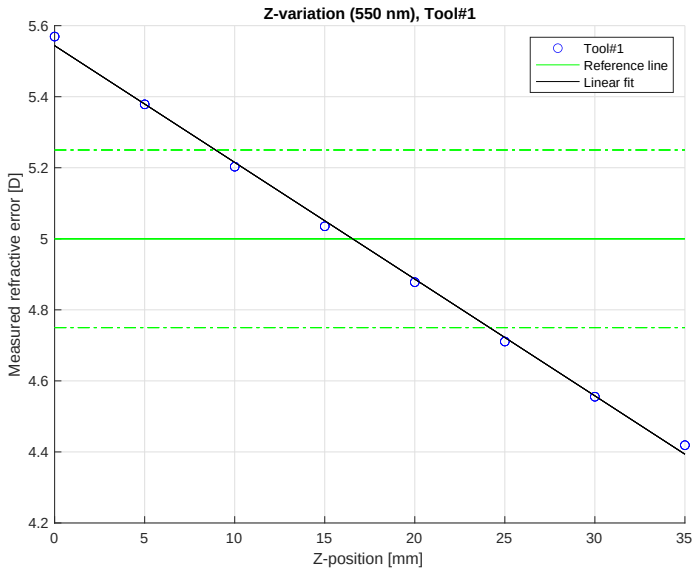

(a) Measured refractive error of Tool#1 for different z-positions. The correct refractive error is obtained at $z \approx 17$ mm.

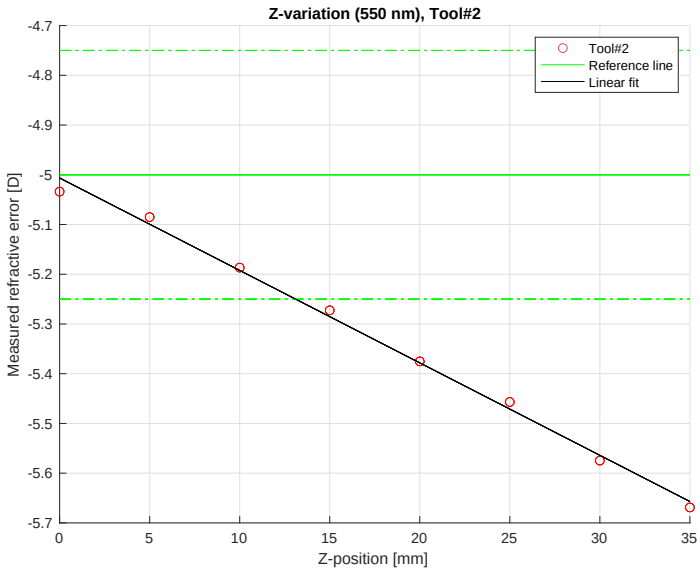

(b) Measured refractive error of Tool#2 for different z-positions. The correct refractive error is obtained at $z \approx 0$ mm.

Figure 4.3: The graphs shows the results from the Z-variation experiment, where the data has been wavelength corrected to 550 nm.

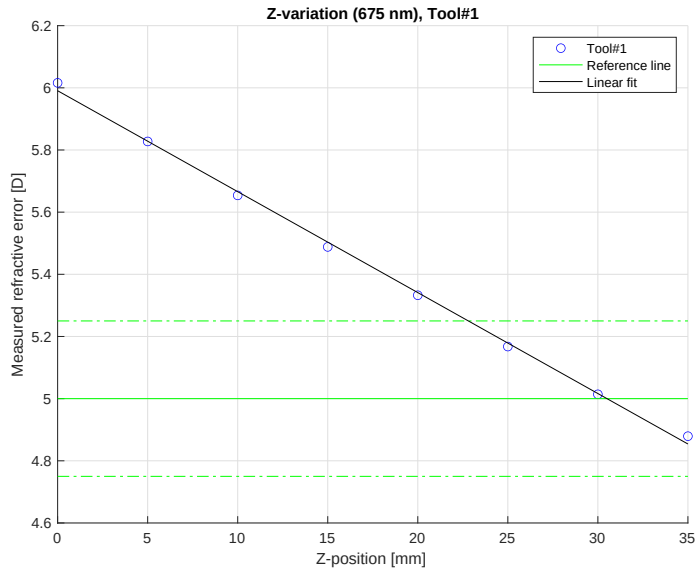

(a) Measured refractive error of Tool#1 for different z-positions. The correct refractive error is obtained at $z \approx 30.5$ mm.

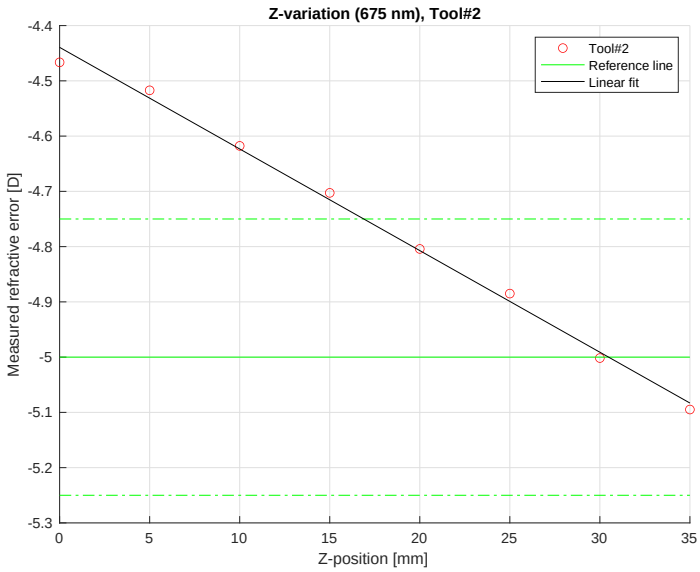

(b) Measured refractive error of Tool#2 for different z-positions. The correct refractive error is obtained at $z \approx 30.5$ mm.

Figure 4.4: The graphs shows the results from the Z-variation experiment, where the data has been wavelength corrected to 675 nm. Tool#1 and Tool#2 share the same correct z-position of 30.5 mm for this wavelength correction.

unfortunately the focal length of the lenslet array used in the HSWS is not known. A focal length of 4.1 mm was assumed, based on the HSWS used in the dual-angle system (manufactured by Thorlabs, part number WFS30-5C). The lenslet array was assumed to be made from BK7 and consist of several 1 mm thick square equiconvex lenses.

The simulations clearly showed that the sharpest image on the sensor is *not* when the image falls onto the first surface of the lenslet array. The sharpest image instead occurs when the image is behind the lenslet array, close to the sensor. The converging cone of rays hits several lenslets, but the spots from the lenslets coincides on the sensor, see Figure 4.6. The simulations also showed that even when the telescope focuses a point source exactly onto the first surface of the lenslet array, the thickness of the lenslets means we will inevitably hit multiple lenslets. We would thus see multiple spread-out spots from multiple lenslets over a large area on the sensor, which was noted during the tests with equal pupil sizes (see Figure 3.9b). Even if the lenslets were much thinner than in the simulation, the IR spot imaged in Figure 3.9b had a diameter of 1 mm, so its image would hit multiple lenslets on the lenslet array and thus produce multiple spots. Images from the simulations for correct z-position are all shown in Figure 4.5.

The z-shift for the best focus on the detector compared to the correct position was $\Delta z = 3.75$ mm in the image plane, which can be seen in Figure 4.6. This z-shift in the image plane corresponds to a $-\Delta z/M^2$ shift in the object plane. With $M = 2.5$ we get a z-shift of -23.5 mm in the object plane, i.e. the sharpest image is when the eye is 23.5 mm too close to the telescope. This value is remarkably similar to what was observed during the tests, where a z-difference of roughly 2 cm was observed between the tests with equal pupil size and best focus.

We can now check whether our calculated z-shift of 23.5 mm explains the bend in the curve we saw in Figure 4.1a. We do this by correcting the wavelength down to 675 nm and adding an additional plot showing the expected measured refractive error if the eye models had been placed 23.5 mm too close to the telescope (as we suspect they were). A shift in z-position from the correct position would lead to a change in measured refractive error according to the following equation:

$$P_{measured} = \frac{1}{\frac{1}{P_{actual}} + d}, \tag{4.2}$$

where d is the z-shift. The result can be seen in Figure 4.7a. The measured values follow the new plot well, with only slight deviations from the theoretical shift. Wavelength correcting the measurements from 'Trial lenses: equal pupils' to 675 nm yields a graph that follows the theoretical values satisfactorily, see Figure 4.7b. This demonstrates that the wavefront sensor works as expected, as long as the eye models are placed in the correct z-position.

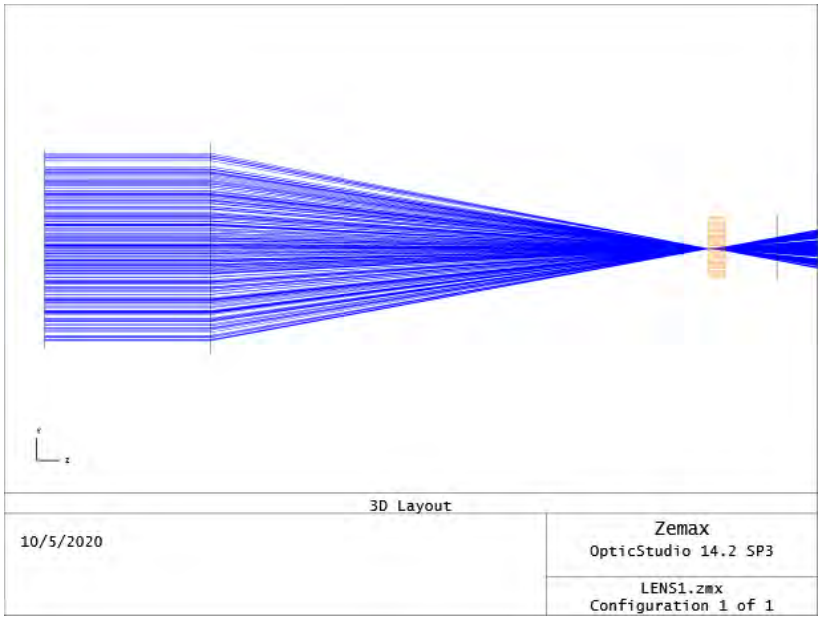

(a) Schematic drawing showing the second lens of the telescope, the lenslet array and the camera detector.

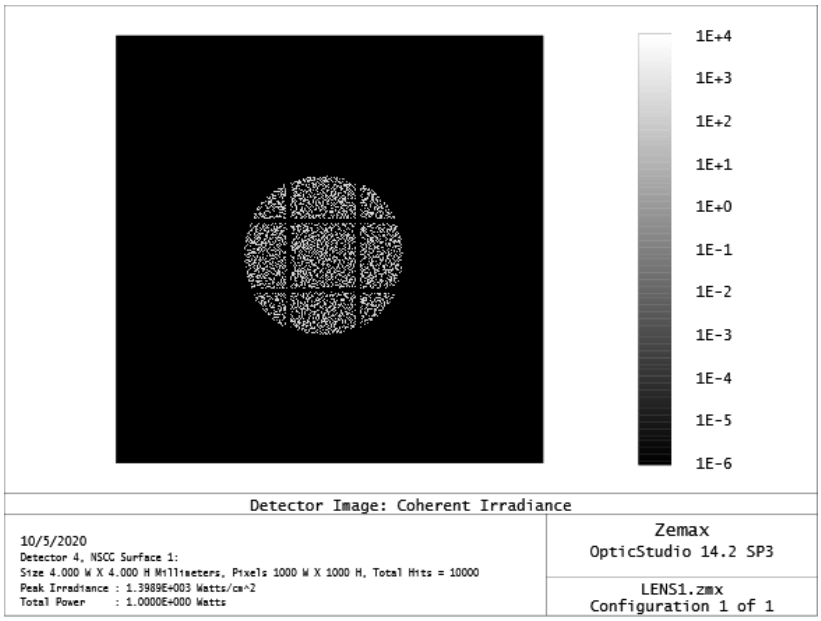

(b) Output from the camera detector. We see spots from multiple lenslets, and the total spot radius is quite large.

Figure 4.5: Zemax simulation for correct z-position, where the point source is focused exactly onto the lenslet array.

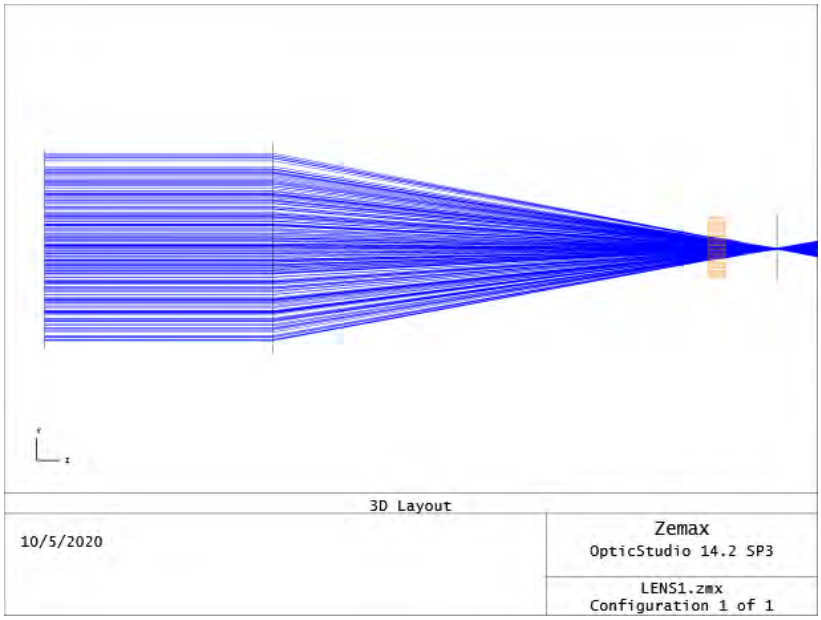

(a) Schematic drawing showing the second lens of the telescope, the lenslet array and the camera detector.

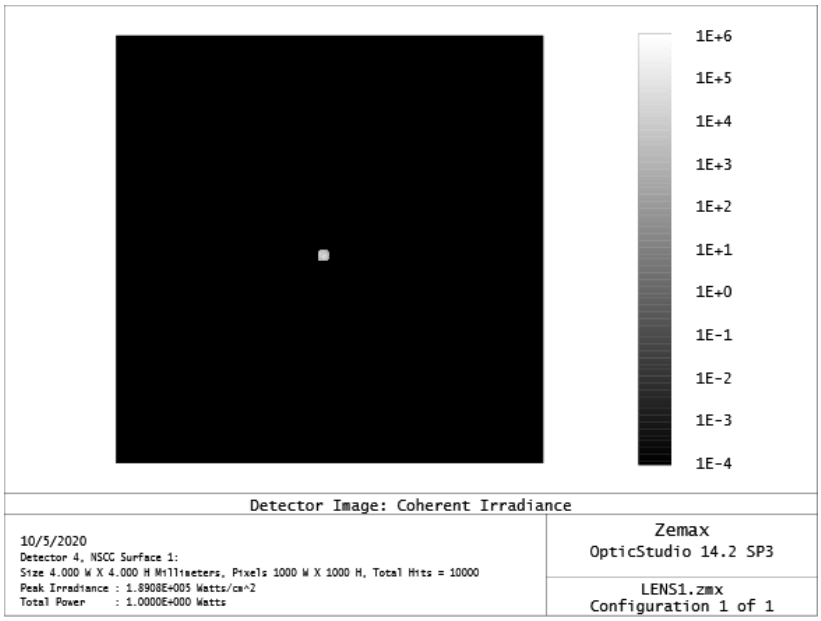

(b) Output from the camera detector. Spots from multiple lenslets coincide on the detector.

Figure 4.6: Zemax simulation for sharpest image, where the telescope has been offset 3.75 mm from the correct position.

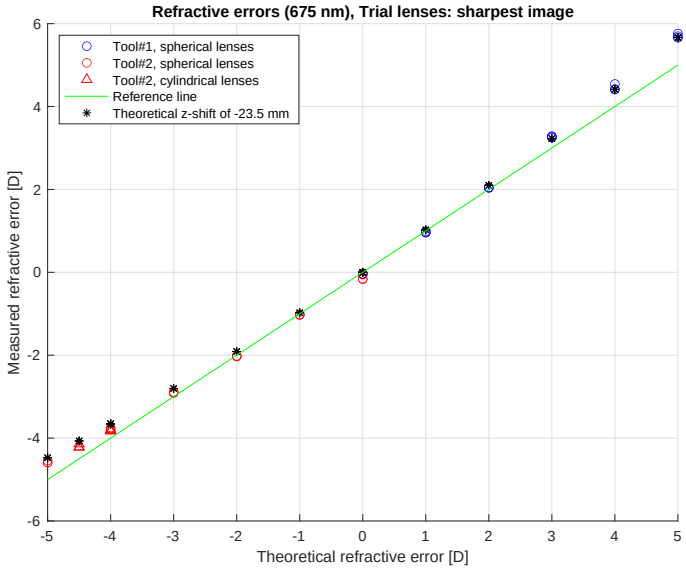

(a) Measurements for the first experiment (Trial lenses: sharpest image), where the data has been wavelength corrected to 675 nm. The black asterisks show the expected bend in the curve if the eye model was 23.5 mm too close to the telescope.

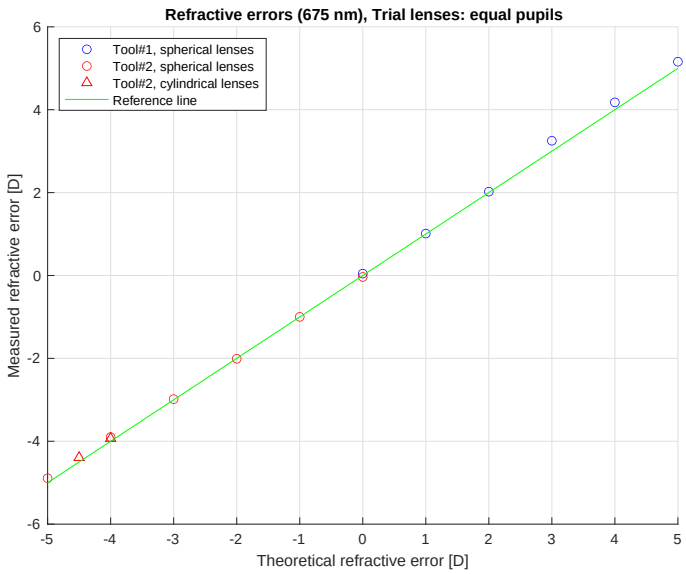

(b) Measurements for the second experiment (Trial lenses: equal pupils), where the data has been wavelength corrected to 675 nm. The data points follow the expected values reasonably well.

Figure 4.7: Graphs of measured vs. theoretical refractive error, after wavelength correction to 675 nm.

4.2 Human eye tests

The measured Zernike coefficients from the measurements on the test subjects were wavelength corrected to $\lambda = 550$ nm according to normal eye dispersion. The pupil sizes were normalised to be 4 mm in diameter.

The equation for mean sphere error was used to calculate the refractive error:

$$\text{Mean sphere [D]} = -\frac{4\sqrt{3}C_2^0}{r^2} + \frac{12\sqrt{5}C_4^0}{r^2} - \frac{24\sqrt{7}C_6^0}{r^2}, \tag{4.3}$$

where r is the pupil radius and C_2^0, C_4^0 and C_6^0 are the normalised Zernike coefficients for defocus, primary spherical aberration and secondary spherical aberration, respectively. [17, 18]

The measured refractive error for the test subjects can be found in Table 4.1. Test subjects 1 and 2 are emmetropes and should thus have a refractive error of 0 D, whereas subject 3, who is myopic, should have a refractive error of -2 D. However, as there was no illuminated focusing target, the level of accommodation in each subject is unknown and is most likely the main reason the measured refractive errors are off from what we might have expected. For example, if the subject focused on the wall which was 130 cm away, we would get a refractive error of -0.77 D. If the subject focused even closer, for instance on the pupil camera, the error would be even more negative. For this reason the measured refractive errors can't be properly compared to what we would expect.

Test subject	**Test run**	**Refractive error**
1	Run 1, fovea	-1.89 D
2	Run 1, fovea	-0.38 D
	Run 2, fovea	-0.20 D
	Run 3, fovea	-0.20 D
3	Run 1, fovea	-3.24 D
	Run 2, fovea	-3.35 D
	Run 3, fovea	-3.39 D
	Run 4, periphery	-2.03 D

Table 4.1: Measured refractive error of the test subjects.

Even though the refractive errors were off from what we would expect for relaxed eyes, the tests were still a success since we were actually able to measure on humans with readable data. The test runs on subject 3 showed that temporal peripheral horizontal coma (C_3^1) had the correct sign (+), as did the foveal primary spherical aberration (also +). The foveal astigmatism was also correctly oriented. This indicates that the coordinate system transformation during the analysis was correct.

A few things about the setup that hadn't been noticed during the eye model tests were discovered. The laser spot on the retina had a striped interference pattern, which it should not have. This turned out to be because of a double reflection

from the hot mirror, producing two parallel beams into the eye. The beams focus to the same spot on the retina and produce the interference pattern. The extra reflection was from the back side of the hot mirror, which doesn't seem to have an anti-reflex coating. The front side of the hot mirror also had a lower reflectivity at $\lambda = 830$ nm than what was specified, roughly 25% rather than the specified 74%. This resulted in that the reflected beam from the back of the mirror was strong enough to produce a visible interference pattern on the retina.

The laser beam transmitted through the beam-splitter was just a few millimetres clear of the head of the test subject. This beam was now also stronger than the one from the hot mirror. Sometimes it accidentally hit the hairs or ear of the test subject and was reflected back to the sensor, which interfered with the detection of the wavefront from the eye. This is clearly sub-optimal.

4.3 Future improvements

Though it was possible to find the correct position for the eye models, this was only because we had two models with the same aperture size next to each other at the same z-position. This made it easy to simply slide the wavefront sensor along the optical rail to compare the measured pupil sizes for the two eye models. For a human eye that changes pupil sizes all the time, this is not be possible. Since the HSWS can't be used to find the correct position of the eye, it follows that this compact wavefront sensor can't be used by itself, the way it is now, to measure human eyes. An additional pupil camera is necessary to judge the correct position of a human eye.

For the tests on human eyes the pupil camera was placed behind the hot mirror and focused to the correct position (found with the eye models). However, it would be better to place the pupil camera in a way that doesn't block the field-of-view.

A beam-splitter between the lenses of the telescope is normally used to redirect light to a pupil camera. In a 4f-Kepler setup, the image of the pupil will be at infinity after the first lens and can be imaged by most camera lenses (which can normally image objects that are between infinity and a few decimetres away). However, in the 2f-Kepler setup, the image of the telescope will not be at infinity after the first lens. Instead, the image of the pupil is positioned roughly 13 centimetres after the first lens, which might be only a few centimetres either in front of or behind the pupil camera, if we want the pupil camera to be close to the telescope. Most camera lenses will thus not work for imaging the pupil onto the pupil camera. There are a few alternatives for how to focus the image onto the pupil camera:

- Find a camera lens for the pupil camera that is able to focus the image of the pupil onto the camera, even though the image is very close to the pupil camera. The choice of camera lens will depend on where the camera is placed relative to the intermediate image formed by the first lens.

- Use a second lens after the beam-splitter that images the pupil to infinity. Then use a standard pupil camera and camera lens to image the pupil.
- Image the pupil directly onto the pupil camera sensor with the first lens, without any additional focusing optics. This option is the simplest, but we are limited to the magnification and depth of field provided by the first lens.
- Place the pupil camera further away from the telescope so that a standard pupil camera and camera lens can be used.

Regardless of which option for pupil camera and lens is chosen, the system will inevitably get larger. We will face the same problems for fixing the pupil camera (and eventual focusing optics) to the cage system as we did for the HSWS. If the pupil camera is too heavy or too far away from the rest of the cage system it will also have to be supported from below, making our system more difficult to move and mount. The choice of pupil camera, additional optics and mounting will require careful consideration and calculation, and is beyond the scope of this thesis.

When a pupil camera is used to find the correct eye position, a diaphragm could be placed at the common focal point of the telescope lenses to limit stray light to the HSWS.

The hot mirror currently used in the final setup turned out to be sub-optimal. For more natural viewing conditions through the hot mirror and better reflectivity, a dichroic mirror with a cutoff between visible and near-IR light should be used instead.

A beam-dump or mirror should be placed at the near exit to the beam-splitter, both for safety for the test subject and to reduce the risk for interfering reflections.

The telescope rods can be shortened even more to enable longer rods between the hot mirror and beam-splitter, providing extra space between the test subject and the beam-dump/mirror for the laser beam.

Chapter 5

Conclusion

The constructed wavefront sensor was able to correctly measure the refractive errors and pupil sizes of eye models, when the eye models were placed at the correct z-position. It was also possible to measure on human eyes in the central and peripheral visual field. This demonstrates that it is possible to reduce the size of an open-field wavefront sensor by not using a 4f telescope. The telescope design used in this system is still a simple two-lens Keplerian telescope, though of a reduced length and not placed in 4f configuration.

Compared to a 4f-Kepler system, the 2f-Kepler design enables a much shorter system length. The drawback is that it is harder to find the correct position of the eye with a 2f-Kepler design. Once the correct position has been found though, the 2f-Kepler system is not more difficult to use than a 4f-Kepler system. Both systems need pupil cameras to properly align eyes in the z-direction, as the HSWS can not be used to find the correct position.

The aim of this thesis was to produce a more compact and portable ocular wavefront sensor. This was obtained by reducing the size of the telescope, and by being constructed as a single unit. The wavefront sensor was easy to slide back and forth along an optical rail, and should also be easy to move to another optical rail without the need for realignment.

Acknowledgements

Firstly, I want to express my deepest thanks to my supervisors. I will always be grateful towards Linda Lundström, whose encouragement, ideas, guidance and feedback have helped me during all stages of my work. I want to thank Dmitry Romashchenko, whose generous feedback, experience, insights and practical tips have helped me tremendously. You've both been the most kind and helpful supervisors I could ever have asked for. Thank you.

I would also like to thank the other members of the visual optics group, Peter Unsbo and Petros Papadogiannis, for lending me their time and expertise whenever I needed help. Many thanks also go to the rest of the BioX group, for help with various tasks and for providing such a positive work environment.

Lastly, I would like to thank my friends and family for their constant love and support.

Bibliography

[1] J. Liang, B. Grimm, S. Goelz, and J. F. Bille, "Objective measurement of wave aberrations of the human eye with the use of a hartmann–shack wave-front sensor," *J. Opt. Soc. Am. A*, vol. 11, pp. 1949–1957, Jul 1994.

[2] G. Dai, *Wavefront Optics for Vision Correction*. Bellingham: SPIE, 2008.

[3] "Image: Schematic diagram of the human eye en." https://commons.wikimedia.org/wiki/File:Schematic_diagram_of_the_human_eye_en.svg#file. Accessed 2020-04-13. License: CC BY-SA 3.0.

[4] "Image: Encyclopædia britannica." https://www.britannica.com/technology/astigmatism-optics/images-videos#/media/1/39798/62039. Accessed 2020-04-13.

[5] "Image: Spherical aberration 2." https://commons.wikimedia.org/wiki/File:Spherical_aberration_2.svg. Accessed 2020-04-13. License: public domain.

[6] "Image: Lens-coma." https://commons.wikimedia.org/wiki/File:Lens-coma.svg. Accessed 2020-04-13. License: CC BY-SA 3.0.

[7] "Image: Shack-hartmann." https://commons.wikimedia.org/wiki/File:Shack_hartmann.jpg. Accessed 2020-03-20. License: CC BY-SA 3.0.

[8] B. Dörband, *Handbook of optical systems. 5, Metrology of optical components and systems*, pp. 188–189. Weinheim: Wiley-VCH, 2005.

[9] E. Hecht, *Optics*. Pearson Education Limited, 2014.

[10] E. J. Sarver, "Compact ocular wavefront system with long working distance," 2010. US Patent Application 2010/0208203 A1.

[11] "Haso 32 wavefront sensor datasheet from Imagine Eyes." https://www.imagine-eyes.com/wp-content/uploads/2014/08/M-DCP-009-e-HASO-32-eye-datasheet.pdf. Accessed 2020-08-25.

[12] D. Romashchenko and L. Lundström, "Dual-angle open field wavefront sensor for simultaneous measurements of the central and peripheral human eye," *Biomedical optics express*, vol. 11, no. 6, p. 3125, 2020.

[13] "Declaration of helsinki," tech. rep., World Medical Association, 2013.

[14] "Artificiell optisk strålning," Tech. Rep. AFS 2009:7, Arbetsmiljöverket, 2019.

[15] J. Tarrant, A. Roorda, and C. F. Wildsoet, "Determining the accommodative response from wavefront aberrations," *Journal of Vision*, vol. 10, 2010.

[16] L. Lundström, *Wavefront Aberrations and Peripheral Vision*. PhD thesis, KTH, Applied Physics, 2007. QC 20100809.

[17] "Methods for reporting optical aberrations of eyes," Standard ANSI Z80.28-2004, American National Standards Institute, 2004.

[18] V. N. Mahajan, *Optical imaging and aberrations. Part III, Wavefront analysis*. SPIE, 2013.

[19] "Article on abcd matrix in the RP Photonics Encyclopedia." `https://www.rp-photonics.com/abcd_matrix.html`. Accessed 2020-04-19.

Appendix A

Derivation of ray transfer matrices

The matrix describing free-space propagation over a distance d is [19]

$$D = \begin{bmatrix} 1 & d \\ 0 & 1 \end{bmatrix} \tag{A.1}$$

and the matrix describing a thin lens with focal length f is

$$L = \begin{bmatrix} 1 & 0 \\ -\frac{1}{f} & 1 \end{bmatrix}. \tag{A.2}$$

By combining these we can get the total ray transfer matrix (also known as the ABCD-matrix) of the system.

For a two-lens system the system ray transfer matrix is:

$$S = D_3 L_2 D_2 L_1 D_1 \tag{A.3}$$

Manual calculations of ray transfer matrices is very cumbersome, but thankfully they can be performed easily with computer aid. The following MATLAB script was used to verify that both the 4f-system and a 2f-Kepler system have the same system matrices.

```
%% For 4f-Kepler

syms f1;
syms f2;
syms obj;
syms ima;
syms d;

d = f1+f2;
```

```
%for 4f
obj = f1;
ima = f2;

L1 = [1 0; -1/f1 1];
L2 = [1 0; -1/f2 1];

OBJ = [1 obj; 0 1];
D = [1 d; 0 1];
IMA = [1 ima; 0 1];

TOT = IMA*L2*D*L1*OBJ;
TOT = simplify(TOT);
disp('Ray transfer matrix for 4f Kepler')
disp(TOT)

%% For 2f-Kepler
syms f1;
syms f2;
syms obj;
syms ima;
syms d;

d = f1+f2;

%for 2f-Kepler (from Hecht)
ima = (f2*d - f2*obj*f1/(obj-f1))/(d - f2 - obj*f1/(obj-f1));

L1 = [1 0; -1/f1 1];
L2 = [1 0; -1/f2 1];

OBJ = [1 obj; 0 1];
D = [1 d; 0 1];
IMA = [1 ima; 0 1];

TOT = IMA*L2*D*L1*OBJ;
TOT = simplify(TOT);
disp('Ray transfer matrix for compact Kepler')
disp(TOT)
```

The output when run is

```
Ray transfer matrix for 4f-Kepler
[ -f2/f1,      0]
```

```
[      0, -f1/f2]

Ray transfer matrix for 2f-Kepler
[ -f2/f1,      0]
[      0, -f1/f2]
```

which shows that the two systems have identical optical properties.

Appendix B

Derivation of 2f-Kepler limit

This appendix derives the limit of how compact a 2f-Kepler telescope can be for a fixed eye to first lens distance (s_{o1}).

For a 2f-Kepler telescope the image distance s_{i2} from the second lens is [9]

$$s_{i2} = \frac{f_2 d - f_2 s_{o1} f_1/(s_{o1} - f_1)}{d - f_2 - s_{o1} f_1/(s_{o1} - f_1)}. \tag{B.1}$$

In order to get afocality we need $d = f_1 + f_2$. We also have $f_2 = M_T f_1$, where $M_T = 1/M_a$ is the transverse magnification and M_a is the angular magnification.

The limit to how small we can make the Kepler telescope if we have a set object distance is when $s_{i2} = 0$. We get

$$0 = \frac{f_2 d - f_2 s_{o1} f_1/(s_{o1} - f_1)}{d - f_2 - s_{o1} f_1/(s_{o1} - f_1)} = \frac{f_2(f_1 + f_2) - f_2 s_{o1} f_1/(s_{o1} - f_1)}{(f_1 + f_2) - f_2 - s_{o1} f_1/(s_{o1} - f_1)} = \tag{B.2}$$

$$= \frac{f_2((f_1 + f_2) - s_{o1} f_1/(s_{o1} - f_1))}{f_1 - s_{o1} f_1/(s_{o1} - f_1)} = \frac{M_T f_1((f_1 + M_T f_1) - s_{o1} f_1/(s_{o1} - f_1))}{f_1(1 - s_{o1}/(s_{o1} - f_1)} = \tag{B.3}$$

$$= \frac{M_T f_1^2((1 + M_T) - s_{o1}/(s_{o1} - f_1))}{f_1(1 - s_{o1}/(s_{o1} - f_1))} = \frac{M_T f_1((1 + M_T) - s_{o1}/(s_{o1} - f_1))}{1 - s_{o1}/(s_{o1} - f_1)} \tag{B.4}$$

This means that the nominator must equal zero. We get

$$M_T f_1((1+M_T) - s_{o1}/(s_{o1}-f_1)) = 0 \tag{B.5}$$
$$(1+M_T) - s_{o1}/(s_{o1}-f_1) = 0 \tag{B.6}$$
$$1+M_T = \frac{s_{o1}}{s_{o1}-f_1} \tag{B.7}$$
$$(s_{o1}-f_1)(1+M_T) = s_{o1} \tag{B.8}$$
$$-f_1(1+M_T) = s_{o1} - s_{o1}(1+M_T) \tag{B.9}$$
$$-f_1(1+M_T) = s_{o1}(1-(1+M_T)) \tag{B.10}$$
$$-f_1(1+M_T) = -s_{o1}M_T \tag{B.11}$$
$$f_1 = \frac{s_{o1}M_T}{1+M_T} \tag{B.12}$$

If we now exchange the transverse magnification for angular magnification we get

$$f_1 = \frac{s_{o1}\frac{1}{M_a}}{1+\frac{1}{M_a}} = \frac{s_{o1}}{M_a(1+\frac{1}{M_a})} = \frac{s_{o1}}{M_a+1}. \tag{B.13}$$

This means that for a system with an object distance (to the first lens) of s_{o1} the minimum focal length for the first lens is $f_1 = s_{o1}/(M_a+1)$. The total system length l_{lim} is

$$l_{lim} = s_{o1} + f_1 + f_2 = s_{o1} + f_1 + \frac{f_1}{M_a} = s_{o1} + f_1\left(1+\frac{1}{M_a}\right) = \tag{B.14}$$
$$= s_{o1} + \frac{s_{o1}}{M_a+1}\left(1+\frac{1}{M_a}\right) = s_{o1}\left(1+\frac{1}{M_a+1}\frac{M_a+1}{M_a}\right) = \tag{B.15}$$
$$= s_{o1}\left(1+\frac{1}{M_a}\right). \tag{B.16}$$

Similarly, the length of a 4f-Kepler telescope is

$$l_{4f} = 2f_1 + 2f_2 = 2\left(f_1 + \frac{f_1}{M_a}\right) = 2f_1\left(1+\frac{1}{M_a}\right) \tag{B.17}$$

Note that for a 4f-telescope $s_{o1} = f_1$, so the total length is exactly twice the length of our limited case above, i.e. $l_{4f} = 2l_{lim}$.

Appendix C

List of components in final setup

Description	Part name
By Thorlabs	
Laser diode 830 nm, 10 mW, fiber-coupled	LPS-830-FC
Fiber port, beam diameter = 1.00 mm	PAF2-5B
Achromat, 75 mm focal length	AC254-075-B
Achromat, 30 mm focal length	AC127-030-B
Cage plate with 1" double bore, 30 mm wide	CP35/M
Cube-mounted pellicle beam splitter, 700-900 nm	CM1-BP145B2
Hot mirror, rectangular	FM02R
Cage cube for hot mirror	CM1-DCH/M
Fiber port cage plate	CP08FP/M
Gimbal mount for shifting laser beam	KC45D
Flat displacement window	WG11050
Cage plate with 1/2" bore for lens tube	CP32/M
Lens tube for 1/2" optics, 0.5" long	SM05L05
Spanner wrench for 1/2" retainer rings	SPW603
Short rods between BS and HM	ER1-P4
Blank cage plate for sensor	CP31/M
Rods for telescope	ER6-P4
Rods for laser	ER3-P4
Drop in cage mount for diaphragm	DCP1
ER rod adapters	ERSCB-P4
By Imagine Eyes	
Hartmann-Shack Wavefront Sensor	HASO 32-eye

Table C.1: Components used in the final setup.

TRITA TRITA-SCI-GRU 2020:353